Continuous–Discrete Observation-Based Robust Tracking Control of Underwater Vehicles: Design, Stability Analysis, and Experiments

Auwal Tijjani Shehu, Ahmed Chemori, Sofiane Ahmed-Ali, Vincent Creuze

To cite this version:

Auwal Tijjani Shehu, Ahmed Chemori, Sofiane Ahmed-Ali, Vincent Creuze. Continuous–Discrete Observation-Based Robust Tracking Control of Underwater Vehicles: Design, Stability Analysis, and Experiments. IEEE Transactions on Control Systems Technology, 2023, 31 (4), pp.1477–1492. 10.1109/TCST.2022.3224321 . lirmm-03883697

HAL Id: lirmm-03883697
https://hal-lirmm.ccsd.cnrs.fr/lirmm-03883697v1

Submitted on 4 Dec 2022

This article has been accepted for publication in IEEE Transactions on Control Systems Technology. This is the author's version which has not been fully edited and content may change prior to final publication. Citation information: DOI 10.1109/TCST.2022.3224321

Continuous-Discrete Observation-Based Robust Tracking Control of Underwater Vehicles: Design, Stability Analysis, and Experiments

Auwal Shehu Tijjani, *Member, IEEE,* Ahmed Chemori, *Senior Member, IEEE*, Sofiane Ahmed Ali, and Vincent Creuze

Abstract*—This study addresses the tracking control problem of underwater vehicles using a new robust observation-based control scheme. The advantages of the robust integral of the sign of the error (RISE) control, as well as the saturation function and well-known super-twisting algorithm, have been exploited to design a saturated super-twisting RISE (S$^+$RISE) control scheme. However, the proposed S$^+$RISE method requires continuous state measurements. To resolve this issue, a continuous-discrete time observer (CDO) is proposed, which works in tandem with the proposed controller. The resulting control scheme is known as CDO-S$^+$RISE. In addition to estimating disturbances, the proposed CDO solves the problem of multiple sampling rates of the sensors. To demonstrate the asymptotic stability of the resulting non-observation-based closed-loop dynamics with the proposed S$^+$RISE control scheme, Lyapunov arguments are proposed. Then, the exponential stability of the unperturbed closed loop with the proposed CDO, as well as with the proposed S$^+$RISE controller, is studied based on the Lyapunov–Krasovskii concept. To verify the performance recovery of the overall observation-based closed-loop system CDO-S$^+$RISE (controlled by the proposed S$^+$RISE control scheme), an invariant set $\mathcal{A}_{\mathbb{R}}$ is determined using a composite Lyapunov–Krasovskii functional, which guarantees the convergence of the tracking errors to the origin. Several real-time experimental scenarios were conducted on the *Leonard* underwater vehicle prototype to validate the efficiency and robustness of the proposed CDO-S$^+$RISE scheme.

***Index Terms*—Robust control, continuous-discrete observer, stability analysis, underwater vehicles, real-time experiments.**

I. INTRODUCTION

A Frequent issue always arising within the field of control systems when designing an underwater vehicle is guaranteeing the stability of the vehicle's equilibrium points, despite the presence of anticipated or unanticipated perturbations and uncertainties. Although first-order sliding-mode control (SMC) laws are well known to ensure the stability of the equilibrium points of many systems subjected to disturbances and uncertainties, these techniques require infinite control bandwidths [1]. To resolve this critical problem, a continuous SMC based on a super-twisting algorithm was proposed [2]. In [3], a second-order SMC was developed by redesigning a super-twisting algorithm using saturation functions and backstepping-like techniques. The proposed control method aims to maximize the domain of attraction of nonlinear systems with state constraints. However, the proposed approach has not been experimentally validated in real systems, such as underwater vehicles. A real-time application of super-twisting-based SMC for tracking control of an underwater vehicle can be found in [4]. It is worth noting that the finite-time convergence of the SMC to the desired sliding surface can be easily destroyed by a well-known input delay, which is a feature that may characterize many systems. A static output-feedback SMC based on a singular perturbation technique was proposed in [5] to address the problem related to input delay. Another issue faced by continuous SMC is the wind-up effect when implemented in a physical system with actuator saturation. To address this issue, saturated Lipschitz continuous SMC was introduced in [6]. This controller preserves the bounded control signal property, reducing chattering and attenuating high-magnitude noise from the sensor measurements. The most common assumption used in SMC design is that uncertainties and external disturbances are considered as Lipschitz functions bounded by Lipschitz constants. Based on this assumption, the controller performs well in several cases. However, in a situation with the possible impact of stochastic perturbation, the stability of the SMC cannot be guaranteed. To neutralize the impact of this unbounded perturbation (assumed to have a normal distribution), a stochastic super-twisting SMC was proposed in [7]. This stochastic super-twisting SMC approach can be extended to underwater vehicles to address the effects of stochastic external disturbances and uncertainties [8].

The robust integral of the sign of the error (RISE) control technique is another class of SMC-like techniques that guarantee semi-global asymptotic tracking for nonlinear uncertain systems. For this reason, such a scheme demonstrates robustness towards the effects of bounded additive disturbances; accordingly, it is often used for robotic systems [9]. The main drawback of standard RISE control lies in the integral term, which may grow indefinitely and exceed the mechanical actuator limits in the critical condition of nonlinearities and disturbances. To address this issue, saturated RISE feedback control was proposed in [10]. The saturated RISE scheme incorporates the final control signal into a trigonometric function with well-defined bounds. Despite this good forward step in enhancing the RISE feedback control scheme, the resulting closed-loop system after injecting the saturated RISE contains

Auwal Shehu Tijjani, Ahmed Chemori, and Vincent Creuze are with the LIRMM, University of Montpellier, CNRS, Montpellier, France. (e-mail: atshehu@lirmm.fr; ahmed.chemori@lirmm.fr; vincent.creuze@lirmm.fr)

Sofiane Ahmed Ali is with the IRSEEM, Normandie University, EA-4353, Rouen, France. (e-mail: sofiane.ahmedali@esigelec.fr)

The authors acknowledged the Petroleum Technology Development Fund (PTDF), Nigeria, for first author Ph.D. financial support.

Manuscript received April 19, 2005; revised August 26, 2015.

This article has been accepted for publication in IEEE Transactions on Control Systems Technology. This is the author's version which has not been fully edited and content may change prior to final publication. Citation information: DOI 10.1109/TCST.2022.3224321

some discontinuities. Similar to most of the control schemes in the literature, this control approach requires all the state measurements [11]. From a practical perspective, continuous state measurements are not always available because of technical or economic issues [12]. For instance, an expensive Doppler velocity logger (DVL) used for the velocity measurement of underwater vehicles is not always available for low-cost underwater vehicles.

Indeed, because full-state measurements of physical systems are either too expensive or not possible at any cost in various applications, the ultimate solution is to design a state observer [13]. This technique has often been used to provide full state/disturbance estimations to the control scheme [14]. Therefore, observer design has been an active research area, attracting the interest of researchers and practitioners in the field of control. Accordingly, different observer design techniques have been proposed in the literature for nonlinear systems, as follows: An improved high-gain nonlinear observer was proposed to decrease the gain power of a well-known classical high-gain observer by exploiting linear matrix inequalities (LMI) and a compromise index concept in [13]. Similarly, a state observer based on an LMI technique was developed in [15] to compensate for the effect of bounded disturbances. The extension of this approach to marine robots requires knowledge of disturbance bounds. In many marine applications, disturbances are difficult to measure and their bounds are often unknown. Furthermore, the nonlinearities and delays of the different sensors installed on marine robots complicate the control system design for such systems [16]. Considering this delay issue, a tracking control problem was addressed in [17] for single-vehicle and multi-agent cases. However, in real-time experiments conducted by these researchers, critical scenarios, such as robustness and external disturbance tests, have not been considered.

Thus far, most of the proposed observers have been designed based on the strong assumption that the system output measurements are continuous or sampled at relatively high rates [18]. Following this philosophy, external disturbance observers have been coupled with controllers to improve the tracking performance of underwater vehicles (see, e.g., [19]). However, the performance of continuous observers may be significantly affected by the sampling rate of the system output [20]. Although this issue was highlighted in [13], no experimental test has been conducted. Moreover, a low sampling rate may lead to instability and divergence in a continuous observer [21]. An unknown input-based observer structure was proposed in [22]. However, this approach assumes that the output measurements do not evolve between the two sampling instants, which may not be the case from a practical point of view. In addition, the observer has not been validated in systems characterized by high hydrodynamic effects and uncertainties, such as underwater vehicles. For the observer developed in [23], the measurements of the vehicle's states depend on the vision system, which may fail completely under poor visibility conditions.

In practice, physical systems, such as underwater vehicles, are often equipped with different sensors, each operating at a distinct sampling frequency. This issue has motivated the redesign of continuous observers for many real systems. Motivated and inspired by the previous results of [1], as well as the challenges of extending [1] and [10] to low-cost underwater vehicles, in this work we propose a new robust observation-based control scheme to address the tracking problem of underwater vehicles. More precisely, the main contributions of the present work are as follows:

1) First, we resolve the issue of over/under-estimation of the static gains [1] by using saturation-based nonlinear gains, taking into account the actuators' mechanical limits. This new idea affects the ability of the proposed controller to learn disturbances. For this reason, the well-known super-twisting algorithm is combined with saturation-based nonlinear parameters in our proposed control architecture. Then, a smooth hyperbolic tangent function is used to deal with any chattering phenomenon that may arise. This improves the proposed control scheme compared to both [1] and [10]. Accordingly, the enhanced proposed control scheme is named saturated super-twisting RISE (S^+RISE) control. Another challenge is that, like any other feedback controller, the proposed S^+RISE scheme necessitates continuous state measurements, which are not always feasible in practice due to the high cost or scarcity of suitable sensors. Therefore, we propose a continuous-discrete time observer (CDO) to provide a continuous estimation of the state and the disturbances to the proposed controller. Besides being equipped with inter-sample predictors, to address the problem of asynchronous multi-rate sensors' measurements in [24], the proposed CDO uses optimal gains by exploiting the LMI technique. Compared to [18], the proposed CDO considers less restrictive assumptions, and does not include any discontinuous terms.
2) The Lyapunov and Lyapunov–Krasovskii arguments are proposed to prove the semiglobal asymptotic stability of the resulting non-observation-based closed-loop dynamics and the exponential stability analysis of the unperturbed closed-loop with the proposed CDO (and the proposed S^+RISE control law), respectively. The performance recovery of the overall observation-based closed-loop system CDO-S^+RISE is verified using a composite Lyapunov–Krasovskii functional. This implies a stable marine behavior of the resulting closed-loop system.
3) Different real-time experimental scenarios are conducted and compared to show the efficiency and robustness of the proposed CDO-S^+RISE control scheme.

The remainder of this study is organized as follows. Section II describes the technical features of the *Leonard* underwater vehicle used for real-time experiments as well as its modelling. In Section III, the proposed S^+RISE control design and a stability analysis are presented. Section IV details the design and exponential convergence analysis of the proposed CDO, followed by a performance recovery study of the overall closed-loop system (with CDO-S^+RISE) based on the composite Lyapunov–Krasovskii functional. The obtained scenario-based

TABLE I
MAIN TECHNICAL SPECIFICATIONS OF *LEONARD* UNDERWATER VEHICLE

Components	Specifications/Descriptions
Attitude Sensor	Sparkfun MPU 9250, MEMS 9-axes gyrometer, accelerometer and magnetometer microprocessor.
Depth Sensor	Pressure sensor MS5803-02BA.
Dimensions	75cm (L) × 55cm (W) × 45cm (H).
Sampling Periods	Attitude sensor = 40ms and Depth sensor = 50ms.
Computing Resource	Dell Latitude E6230 Intel Core i7 - 2.9 GHz, 16 GB of RAM, 64 bits Windows 10 OS, Microsoft Visual C++ 2015.
Floatability	9N.
Mass	28kg.
Maximal Depth	100m (range depending on the depth sensor).
Power Consumption	24V, 600W.
Tether	50m in pool configuration.
Thrusters	6-Seabotix BTD150 continuous thrust 2.2kgf each with Syren 10 drivers.

real-time experimental results are detailed and discussed in Section V. Section VI presents some conclusions and possible future extensions of this work.

II. VEHICLE DESCRIPTION AND MODELLING

A. Vehicle Description

The proposed CDO-S$^+$RISE control scheme (designed in Sections III and IV) was implemented and tested in real time using a holonomic underwater vehicle named *Leonard* ROV, available at LIRMM, University of Montpellier, CNRS. Although the technical features of *Leonard* underwater vehicle are described in [4] and [25], we propose revisiting them to clearly demonstrate one of the critical issues addressed in the present work. The vehicle is equipped with six independent propellers, which provide thrust to the vehicle when operated in either the autonomous or shared control mode (i.e., with a human pilot in the loop). *Note that all the proposed contributions in this study are validated in real-time on the Leonard vehicle operating autonomously.* In addition, the positions of the center of buoyancy and gravity were exploited to passively stabilize both the roll (ϕ) and pitch (ϑ) angles of the vehicle around zero (i.e., $\phi \approx \vartheta \approx 0$). Consequently, this property reduces the energy consumption of the vehicles. In spite of the above feature, which may result in some simplifications of the control law design, in this study, we focus on designing the proposed algorithms for all six degrees of freedom (DOF) to stabilize the vehicle autonomously. The vehicle was also equipped with depth and attitude sensors, as shown in TABLE I. It is worth noting that these sensors have *different sampling frequencies*, and this is a critical issue affecting the observer/control algorithm performance, as discussed previously in Section I. The following sections show how this study addresses this issue.

B. Vehicle Modelling

The mathematical representation of underwater vehicles with six degrees of freedom is shared in terms of kinematics and dynamics. This mathematical representation can be achieved by assigning two reference frames to the vehicle, as shown in Fig. 1. The reference frames facilitate the navigation and control of the vehicle and are usually named based on the SNAME (Society of Naval Architects and Marine Engineers) standard [25]:

1) The Earth-fixed or inertial reference frame R_e, is usually located at/near the water surface;
2) The Body-fixed or vehicle reference frame R_b, is generally fixed at the center of volume of the vehicle.

The kinematics and dynamics of the underwater vehicle are as follows.

1) Kinematics: The three dimensional (3D) kinematic formulation relating the time derivatives of the vehicle's position and orientation in R_e with respect to its linear and angular velocities in R_b is expressed as follows:

$$\dot{\boldsymbol{\eta}} = \mathbf{J}(\boldsymbol{\eta})\boldsymbol{\nu} \tag{1}$$

where $\boldsymbol{\eta} = [\boldsymbol{\eta}_1^{\mathrm{T}}\ \boldsymbol{\eta}_2^{\mathrm{T}}]^{\mathrm{T}} = [x\ y\ z\ \phi\ \vartheta\ \psi]^{\mathrm{T}} \in \mathbb{R}^{6\times 1}$ is the vector of position and attitude, $\boldsymbol{\nu} = [u\ v\ w\ p\ q\ r]^{\mathrm{T}} \in \mathbb{R}^{6\times 1}$ denotes the linear and angular velocities vector, and $\mathbf{J}(\boldsymbol{\eta}) \in \mathbb{R}^{6\times 6}$ is the 3D transformation matrix from R_e to R_b, as illustrated in Fig. 1. Furthermore, matrix $\mathbf{J}(\boldsymbol{\eta})$ is formulated as follows [26]:

$$\mathbf{J}(\boldsymbol{\eta}) = \begin{bmatrix} \mathbf{J}_1(\boldsymbol{\eta}_2) & \mathbf{0}_{3\times 3} \\ \mathbf{0}_{3\times 3} & \mathbf{J}_2(\boldsymbol{\eta}_2) \end{bmatrix} \tag{2}$$

where $\mathbf{J}_1(\boldsymbol{\eta}_2)$ and $\mathbf{J}_2(\boldsymbol{\eta}_2)$ are expressed as

$$\mathbf{J}_1(\boldsymbol{\eta}_2) = \begin{bmatrix} c\psi c\vartheta & c\psi s\vartheta s\phi - s\psi c\phi & c\psi s\vartheta c\phi + s\psi s\phi \\ s\psi c\vartheta & s\psi s\vartheta s\phi + c\psi c\phi & s\psi s\vartheta c\phi - c\psi s\phi \\ -s\vartheta & c\vartheta s\phi & c\vartheta c\phi \end{bmatrix} \tag{3}$$

$$\mathbf{J}_2(\boldsymbol{\eta}_2) = \begin{bmatrix} 1 & s\psi t\vartheta & c\psi t\vartheta \\ 0 & c\psi & -s\psi \\ 0 & s\phi/c\vartheta & c\phi/c\vartheta \end{bmatrix} \tag{4}$$

with $cx^\star$, $sx^\star$, and $tx^\star$ denoting $\cos x^\star$, $\sin x^\star$, and $\tan x^\star$ functions respectively, with $x^\star \in \{\phi, \vartheta, \psi\}$.

Remark 1: *The kinematics formulation in (1) may not be defined in some cases, due to a possible singularity in $\mathbf{J}(\boldsymbol{\eta})$, especially when the vehicle is operating at a pitch angle ϑ close to $\pm\frac{\pi}{2}$.*

The real-time experiments conducted in this study considered the case in which the desired pitch was designed to be sufficiently far from the neighborhood of $\vartheta = \pm\frac{\pi}{2}$. Thus, the matrices $\mathbf{J}(\boldsymbol{\eta})$ and $[\mathbf{J}(\boldsymbol{\eta})]^{-1}$ exist and are bounded.

2) Dynamics: The dynamics of underwater vehicles, in accordance with the formulation proposed in [26], can be written as follows in the R_b reference frame:

$$\mathbf{M}\dot{\boldsymbol{\nu}} + \mathbf{C}(\boldsymbol{\nu})\boldsymbol{\nu} + \mathbf{D}(\boldsymbol{\nu})\boldsymbol{\nu} + \mathbf{g}(\boldsymbol{\eta}) = \boldsymbol{\tau} + \boldsymbol{\omega}(t) \tag{5}$$

where $\mathbf{M} \in \mathbb{R}^{6\times 6}$ is the inertia matrix, including both rigid-body and added mass, $\mathbf{C}(\boldsymbol{\nu}) \in \mathbb{R}^{6\times 6}$ is the Coriolis and centripetal matrix, $\mathbf{D}(\boldsymbol{\nu}) \in \mathbb{R}^{6\times 6}$ is the damping matrix, $\mathbf{g}(\boldsymbol{\eta}) \in$

This article has been accepted for publication in IEEE Transactions on Control Systems Technology. This is the author's version which has not been fully edited and content may change prior to final publication. Citation information: DOI 10.1109/TCST.2022.3224321

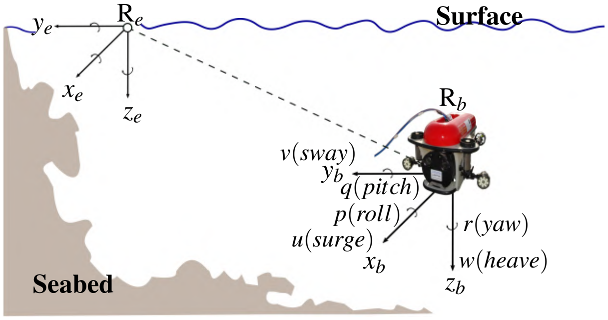

Fig. 1. Illustration of the coordinate systems.

$\mathbb{R}^{6\times1}$ is the vector of gravity and buoyancy, $\boldsymbol{\tau}\in\mathbb{R}^{6\times1}$ is the vector of the control inputs produced by the thrusters, and $\boldsymbol{\omega}(t)\in\mathbb{R}^{6\times1}$ is a time-varying vector representing the disturbances. The techniques for estimating these dynamic parameters in (5) are described in [25].

It is noteworthy that the matrices $\mathbf{M}$ and $\mathbf{C}$ of our vehicle dynamics in (5) are partially known, whereas $\mathbf{D}$ is uncertain. These uncertainties are mainly due to the unmodeled hydrodynamic effects. Hence, it is necessary to consider these uncertainties in the vehicle dynamics (5). Although the dynamics of underwater vehicles are decomposed into nominal and uncertain parts from the literature, not all of the aforementioned uncertainties are considered. Accordingly, we rewrite (5) as follows:

$$\mathbf{M}^{\star}\dot{\boldsymbol{\nu}}+\mathbf{C}^{\star}(\boldsymbol{\nu})\boldsymbol{\nu}+\mathbf{D}^{\star}(\boldsymbol{\nu})\boldsymbol{\nu}+\mathbf{g}^{\star}(\boldsymbol{\eta})=\boldsymbol{\tau}+\boldsymbol{\omega}^{\star}(t) \tag{6}$$

where $\mathbf{M}=\mathbf{M}^{\star}+\Delta\mathbf{M}^{\star},\mathbf{C}=\mathbf{C}^{\star}+\Delta\mathbf{C}^{\star},\mathbf{D}=\mathbf{D}^{\star}+\Delta\mathbf{D}^{\star},\mathbf{g}=\mathbf{g}^{\star}+\Delta\mathbf{g}^{\star}$, which can be generalized as $\{\mathbf{M}^{\star},\ \mathbf{C}^{\star},\ \mathbf{D}^{\star},\ \mathbf{g}^{\star}\}$ being the nominal part (i.e., the true unapproximated value) and $\{\Delta\mathbf{M}^{\star},\ \Delta\mathbf{C}^{\star},\ \Delta\mathbf{D}^{\star},\ \Delta\mathbf{g}^{\star}\}$ the uncertain part (i.e., unknown part). The time-varying disturbance $\boldsymbol{\omega}(t)$ in (5) is combined with the uncertainties and expressed as $\boldsymbol{\omega}^{\star}(t)=-\Delta\mathbf{M}^{\star}\dot{\boldsymbol{\nu}}-\Delta\mathbf{C}^{\star}(\boldsymbol{\nu})\boldsymbol{\nu}-\Delta\mathbf{D}^{\star}(\boldsymbol{\nu})\boldsymbol{\nu}-\Delta\mathbf{g}^{\star}(\boldsymbol{\eta})+\boldsymbol{\omega}(t)$. The dynamics (6) are also transformed and redefined in frame R_e based on (1) as follows:

$$\begin{aligned}\mathbf{M}^{\star}_{\boldsymbol{\eta}}(\boldsymbol{\eta})\ddot{\boldsymbol{\eta}}+\mathbf{C}^{\star}_{\boldsymbol{\eta}}(\boldsymbol{\nu},\boldsymbol{\eta})\dot{\boldsymbol{\eta}}+\mathbf{D}^{\star}_{\boldsymbol{\eta}}(\boldsymbol{\nu},\boldsymbol{\eta})\dot{\boldsymbol{\eta}}+\mathbf{g}^{\star}_{\boldsymbol{\eta}}(\boldsymbol{\eta})=\boldsymbol{\tau}^{\star}_{\boldsymbol{\eta}}(\boldsymbol{\eta})\\+\boldsymbol{\omega}^{\star}_{\boldsymbol{\eta}}(t)\end{aligned} \tag{7}$$

where $\mathbf{M}^{\star}_{\boldsymbol{\eta}}(\boldsymbol{\eta})=\mathbf{J}^{-\mathrm{T}}(\boldsymbol{\eta})\mathbf{M}^{\star}\mathbf{J}^{-1}(\boldsymbol{\eta})$,
$\mathbf{C}^{\star}_{\boldsymbol{\eta}}(\boldsymbol{\nu},\boldsymbol{\eta})=\mathbf{J}^{-\mathrm{T}}(\boldsymbol{\eta})[\mathbf{C}^{\star}(\boldsymbol{\nu})-\mathbf{M}^{\star}\mathbf{J}^{-1}(\boldsymbol{\eta})\dot{\mathbf{J}}(\boldsymbol{\eta})]\mathbf{J}^{-1}(\boldsymbol{\eta})$,
$\mathbf{D}^{\star}_{\boldsymbol{\eta}}(\boldsymbol{\nu},\boldsymbol{\eta})=\mathbf{J}^{-\mathrm{T}}(\boldsymbol{\eta})\mathbf{D}^{\star}(\boldsymbol{\nu})\mathbf{J}^{-1}(\boldsymbol{\eta}),\mathbf{g}^{\star}_{\boldsymbol{\eta}}(\boldsymbol{\eta})=\mathbf{J}^{-\mathrm{T}}(\boldsymbol{\eta})\mathbf{g}^{\star}(\boldsymbol{\eta})$,
$\boldsymbol{\tau}^{\star}_{\boldsymbol{\eta}}(\boldsymbol{\eta})=\mathbf{J}^{-\mathrm{T}}(\boldsymbol{\eta})\boldsymbol{\tau}$, and $\boldsymbol{\omega}^{\star}_{\boldsymbol{\eta}}(t)=\mathbf{J}^{-\mathrm{T}}(\boldsymbol{\eta})\boldsymbol{\omega}^{\star}(t)$.

Furthermore, the dynamic terms (7) satisfy

Property P1 : *The inertia matrix* $\mathbf{M}^{\star}_{\boldsymbol{\eta}}(\boldsymbol{\eta})$ *is symmetric positive definite and satisfies [25]:* $\kappa\|\boldsymbol{\eta}\|^2\leq\boldsymbol{\eta}^{\mathrm{T}}\mathbf{M}^{\star}_{\boldsymbol{\eta}}(\boldsymbol{\eta})\boldsymbol{\eta}=\boldsymbol{\eta}^{\mathrm{T}}\mathbf{M}^{\star}_{\boldsymbol{\eta}}(\boldsymbol{\eta})^{\mathrm{T}}\boldsymbol{\eta}\leq\kappa(\boldsymbol{\eta})\|\boldsymbol{\eta}\|^2$*, where* $\kappa\in\mathbb{R}_{>0}$ *is a positive constant,* $\kappa(\boldsymbol{\eta})\in\mathbb{R}_{>0}$ *is a non-decreasing positive function,* $\|\cdot\|$ *is a standard Euclidean norm of a vector and matrix, and* $\boldsymbol{\eta}\in\mathbb{R}^{6\times1}$ *(vehicle's trajectory).*

Property P2 : *The matrix* $\mathbf{C}^{\star}_{\boldsymbol{\eta}}(\boldsymbol{\nu},\boldsymbol{\eta})$ *can always be parameterized as,* $\mathbf{C}^{\star}_{\boldsymbol{\eta}}(\boldsymbol{\nu},\boldsymbol{\eta})=-\mathbf{C}^{\star}_{\boldsymbol{\eta}}(\boldsymbol{\nu},\boldsymbol{\eta})^{\mathrm{T}},\ \forall\boldsymbol{\nu},\boldsymbol{\eta}\in\mathbb{R}^{6\times1}$ *[26].*

Property P3 : *The damping matrix* $\mathbf{D}^{\star}_{\boldsymbol{\eta}}(\boldsymbol{\nu},\boldsymbol{\eta})$ *is strictly positive [26], i.e.,* $\boldsymbol{\eta}^{\mathrm{T}}\mathbf{D}^{\star}_{\boldsymbol{\eta}}(\boldsymbol{\nu},\boldsymbol{\eta})\boldsymbol{\eta}>0,\ \forall\boldsymbol{\nu},\boldsymbol{\eta}\neq0\in\mathbb{R}^{6\times1}$.

Property P4 : *The vector* $\mathbf{g}^{\star}_{\boldsymbol{\eta}}(\boldsymbol{\eta})$ *is continuous and bounded, if* $\boldsymbol{\eta}$ *and* $\boldsymbol{\nu}$ *are bounded [26].*

Property P5 : *The inherent actuators' saturation bounds the vehicle thrusters' velocity by a positive constant [25], i.e.,* $\left|\boldsymbol{\tau}^{\star}_{\boldsymbol{\eta}}(\boldsymbol{\eta})_i\right|\leq\kappa^{\star}$*, where* $i=\overline{1,6}$*,* $|\cdot|=$ *absolute value, and* $\kappa^{\star}\in\mathbb{R}_{>0}$ *is a known positive constant.*

To simplify the autonomous control algorithm design for underwater vehicles, the following assumptions were considered.

Assumption A1 : *The disturbance vector* $\boldsymbol{\omega}^{\star}_{\boldsymbol{\eta}}(t)$ *is assumed to be bounded [4], i.e.,* $\left|\boldsymbol{\omega}^{\star}_{\boldsymbol{\eta}}(t)_i\right|\leq\underline{\kappa}^{\star}$*, with* $i=\overline{1,6}$ *and* $\underline{\kappa}^{\star}\in\mathbb{R}_{>0}$.

Assumption A2 : *In the conducted real-time experiments, our vehicle moves at a low speed* ($\leq 0.5ms^{-1}$ *[27]). Hence, the effects of Coriolis and centripetal forces are neglected [25].*

Therefore, based on assumption **A2**, the dynamics (7) can be rewritten as follows:

$$\begin{aligned}\ddot{\boldsymbol{\eta}}=-[\mathbf{M}^{\star}_{\boldsymbol{\eta}}(\boldsymbol{\eta})]^{-1}\dot{\boldsymbol{\eta}}+[\mathbf{M}^{\star}_{\boldsymbol{\eta}}(\boldsymbol{\eta})]^{-1}\boldsymbol{\tau}^{\star}_{\boldsymbol{\eta}}(\boldsymbol{\eta})\\+[\mathbf{M}^{\star}_{\boldsymbol{\eta}}(\boldsymbol{\eta})]^{-1}[\boldsymbol{\omega}^{\star}_{\boldsymbol{\eta}}(t)+\dot{\boldsymbol{\eta}}-\mathbf{D}^{\star}_{\boldsymbol{\eta}}(\boldsymbol{\nu},\boldsymbol{\eta})\dot{\boldsymbol{\eta}}-\mathbf{g}^{\star}_{\boldsymbol{\eta}}(\boldsymbol{\eta})]\end{aligned} \tag{8}$$

Next, we can express (1) and (8) in a state-space form to facilitate the design of the proposed observer introduced in Section IV. To this end, the following state variables are defined.

$$\boldsymbol{\chi}_1(t)=\boldsymbol{\eta},\qquad\boldsymbol{\chi}_2(t)=\dot{\boldsymbol{\eta}} \tag{9}$$

By substituting (9) into (1) and (8), the state-space representation of the underwater vehicle can be obtained as follows:

$$\dot{\boldsymbol{\chi}}(t)=\mathbf{A}_{\boldsymbol{\chi}(t)}\boldsymbol{\chi}(t)+\mathbf{B}_{\boldsymbol{\chi}(t)}\mathbf{u}(t)+\mathbf{D}\boldsymbol{\delta}(t) \tag{10}$$

where $\boldsymbol{\chi}(t)=[\boldsymbol{\chi}_1(t)^{\mathrm{T}}\quad\boldsymbol{\chi}_2(t)^{\mathrm{T}}]^{\mathrm{T}}$, $\boldsymbol{\delta}(t)=\boldsymbol{\omega}^{\star}_{\boldsymbol{\eta}}(t)+\dot{\boldsymbol{\eta}}-\mathbf{D}^{\star}_{\boldsymbol{\eta}}(\boldsymbol{\nu},\boldsymbol{\eta})\dot{\boldsymbol{\eta}}-\mathbf{g}^{\star}_{\boldsymbol{\eta}}(\boldsymbol{\eta})$, $\mathbf{u}(t)=\boldsymbol{\tau}^{\star}_{\boldsymbol{\eta}}(\boldsymbol{\eta})$, $\mathbf{D}=\begin{bmatrix}\mathbf{0}_{6\times6} & [\mathbf{M}^{\star}_{\boldsymbol{\eta}}(\boldsymbol{\eta})]^{-1}\end{bmatrix}^{\mathrm{T}}$, $\mathbf{A}_{\boldsymbol{\chi}(t)}=\begin{bmatrix}\mathbf{0}_{6\times6} & \mathbf{I}_{6\times6}\\ \mathbf{0}_{6\times6} & -[\mathbf{M}^{\star}_{\boldsymbol{\eta}}(\boldsymbol{\eta})]^{-1}\end{bmatrix}$, and $\mathbf{B}_{\boldsymbol{\chi}(t)}=\begin{bmatrix}\mathbf{0}_{6\times6}\\ [\mathbf{M}^{\star}_{\boldsymbol{\eta}}(\boldsymbol{\eta})]^{-1}\end{bmatrix}$.

Finally, dynamics (10) can be rewritten as follows:

$$\dot{\boldsymbol{\chi}}(t)=\tilde{\mathbf{A}}\boldsymbol{\chi}(t)+\tilde{\mathbf{B}}_{\boldsymbol{\chi}(t)}\mathbf{u}(t)+\tilde{\mathbf{D}}\boldsymbol{\delta}^{\star}(t) \tag{11}$$

where $\tilde{\mathbf{A}}=\begin{bmatrix}\mathbf{0}_{6\times6} & \mathbf{I}_{6\times6}\\ \mathbf{0}_{6\times6} & \mathbf{0}_{6\times6}\end{bmatrix}$, $\tilde{\mathbf{B}}_{\boldsymbol{\chi}(t)}=\mathbf{B}_{\boldsymbol{\chi}(t)}$, $\tilde{\mathbf{D}}=\begin{bmatrix}\mathbf{0}_{6\times6}\\ \mathbf{I}_{6\times6}\end{bmatrix}$, $\boldsymbol{\delta}^{\star}(t)=[\mathbf{M}^{\star}_{\boldsymbol{\eta}}(\boldsymbol{\eta})]^{-1}[\boldsymbol{\delta}(t)-\boldsymbol{\chi}_2(t)]$.

III. PROPOSED CONTROL LAW DESIGN AND STABILITY ANALYSIS

A. Control Law Design

This section presents the design of the proposed S^{+}RISE for trajectory tracking. Although the RISE feedback control proposed in [1] provides good performance, several challenges are encountered when implementing such a control scheme in real time on low-cost underwater vehicles. First, the vehicle used to implement the control in [1] is equipped with various sensors (including DVL, GPS receiver, and sonar) that the controller can exploit. However, not all of these sensors are available for underwater vehicles (especially low-cost vehicles) because of their high cost. In addition to the static feedback gains in the control scheme structure, the inherent saturations of the vehicle's mechanical actuators are not taken into account.

Furthermore, the authors of [1] proposed adding a dynamics-based feedforward term to the system dynamics to improve the control scheme performance; however, obtaining accurate dynamics remains a challenging task.

Guided by the above issues and inspired by [10], we propose redesigning the RISE control scheme of [1] to address these problems. First, the static feedback gains are transformed into saturation-based nonlinear gains in the RISE feedback controller proposed in [1] to avoid overestimation or underestimation of the gains within the admissible limits of the actuators. This step is followed by a critical challenge in introducing saturation limits in robust terms without affecting their ability to learn the disturbances. To this end, we propose redesigning the robust term of the RISE controller in [1] using the well-known super-twisting algorithm. Following that, we replace the algorithm's static gain with a saturation-based nonlinear gain to improve its robustness. Furthermore, a smooth hyperbolic tangent function is used in the proposed S$^+$RISE control scheme instead of the conventional sign function, which deals with any discontinuity that may arise in this approach. The proposed S$^+$RISE controller is designed as follows:

Let us first consider $\boldsymbol{\eta}_d(t)$ and $\boldsymbol{\eta}(t)$ as the desired and actual vehicle trajectories, respectively, which are defined as follows:

$$\begin{aligned}\boldsymbol{\eta}_d(t) &= [x_d(t), y_d(t), z_d(t), \phi_d(t), \vartheta_d(t), \psi_d(t)]^{\mathrm{T}} \\ \boldsymbol{\eta}(t) &= [x(t), y(t), z(t), \phi(t), \vartheta(t), \psi(t)]^{\mathrm{T}}\end{aligned} \tag{12}$$

The desired trajectory satisfies the following assumption.

Assumption A3 : *The time derivatives of* $\boldsymbol{\eta}_d$ *(i.e.,* $\dot{\boldsymbol{\eta}}_d, \cdots, \dddot{\boldsymbol{\eta}}_d$*) are assumed to be smooth and bounded by design.*

The vehicle-tracking error $\mathbf{e}_1(t)$ and its first-time derivative are defined as follows:

$$\mathbf{e}_1(t) = \boldsymbol{\eta}_d(t) - \boldsymbol{\eta}(t),\ \dot{\mathbf{e}}_1(t) = \dot{\boldsymbol{\eta}}_d(t) - \dot{\boldsymbol{\eta}}(t) \tag{13}$$

where $\dot{\boldsymbol{\eta}}_d(t)$ and $\dot{\boldsymbol{\eta}}(t)$ are the first time derivatives of $\boldsymbol{\eta}_d(t)$ and $\boldsymbol{\eta}(t)$, respectively, $\mathbf{e}_1(t) = [e_{11}(t), e_{12}(t), \cdots, e_{16}(t)]^{\mathrm{T}}$, and $\dot{\mathbf{e}}_1(t) = [\dot{e}_{11}(t), \dot{e}_{12}(t), \cdots, \dot{e}_{16}(t)]^{\mathrm{T}}$.

We can now design a measurable auxiliary tracking error $\mathbf{e}_2(t)$ using a smooth bounded function of $\mathbf{e}_1(t)$, as follows:

$$\mathbf{e}_2(t) = \dot{\mathbf{e}}_1(t) + \boldsymbol{\alpha}\tanh[\mathbf{e}_1(t)] \tag{14}$$

where $\boldsymbol{\alpha} = diag\{\alpha_1, \alpha_2, \cdots, \alpha_6\} > 0$, defines the rate of convergence of $\dot{\mathbf{e}}_1(t)$, $\mathbf{e}_2(t) = [e_{21}(t), e_{22}(t), \cdots, e_{26}(t)]^{\mathrm{T}}$, and tanh is a hyperbolic tangent function.

Based on the closed-loop stability guarantee (cf. stability analysis subsection), the proposed S$^+$RISE control law can be designed for the six degrees of freedom of the vehicle as follows:

$$\begin{aligned}\boldsymbol{\tau} = \mathbf{J}^{\mathrm{T}}(\boldsymbol{\eta})\Big[&(\mathbf{K}(\cdot)+\mathbf{I})\mathbf{e}_2(t) - (\mathbf{K}(t_0)+\mathbf{I})\mathbf{e}_2(t_0) \\ &+ \int_{t_0}^{t}[\boldsymbol{\varphi}(\sigma) + \boldsymbol{\varphi}^{\star}(\sigma)]d\sigma\Big]\end{aligned} \tag{15}$$

where $\boldsymbol{\varphi}(\sigma)$ and $\boldsymbol{\varphi}^{\star}(\sigma)$ are the robust terms of the proposed S$^+$RISE control scheme, $\boldsymbol{\tau} \in \mathbb{R}^{6\times1}$ is the control input vector, $\mathbf{I} \in \mathbb{R}^{6\times6}$ is the identity matrix, and $\mathbf{J}(\boldsymbol{\eta}) \in \mathbb{R}^{6\times6}$ is defined by (1). The second term, $(\mathbf{K}(t_0)+\mathbf{I})\mathbf{e}_2(t_0)$ in (15), ensures that $\boldsymbol{\tau}(t_0) = 0$, where t_0 is the initial time.

And if we consider a scalar case of $\boldsymbol{\varphi}(\sigma)$ and $\boldsymbol{\varphi}^{\star}(\sigma)$, the following expressions are formulated for $\boldsymbol{\varphi}_i(\sigma)$ and $\boldsymbol{\varphi}_i^{\star}(\sigma)$:

$$\begin{aligned}\boldsymbol{\varphi}_i(\sigma) &= (\mathbf{K}_i(\cdot)+1)\boldsymbol{\Lambda}_i(\cdot)\tanh[\mathbf{e}_{2i}(\sigma)] \\ \boldsymbol{\varphi}_i^{\star}(\sigma) &= \mathbf{B}_i(\cdot)\Big[\frac{\mu_{1i}^2}{2}\tanh[\mathbf{e}_{2i}(\sigma)] + \mu_{2i}^2\mathbf{e}_{2i}(\sigma) \\ &+ \frac{3\mu_{1i}\mu_{2i}}{2}\big|\mathbf{e}_{2i}(\sigma)\big|^{0.5}\tanh[\mathbf{e}_{2i}(\sigma)]\Big],\quad i = \overline{1,6}\end{aligned} \tag{16}$$

where $\mu_{1i} > 0$ and $\mu_{2i} > 0$ are positive design constants and $\mathbf{K}_i(\cdot)$, $\mathbf{B}_i(\cdot)$, and $\boldsymbol{\Lambda}_i(\cdot)$ are the parameters of the proposed controller. Furthermore, the parameters in (15)–(16) are formulated as follows.

$$\begin{aligned}\mathbf{K}_i(\cdot) &= \begin{cases} k_{0i}\big|\mathbf{e}_{2i}(t)\big|^{(\delta_{1i}-1)} & \text{if} \quad \big|\mathbf{e}_{2i}(t)\big| > \varepsilon_{1i} \\ k_{0i}\varepsilon_{1i}^{(\delta_{1i}-1)} & \text{if} \quad \big|\mathbf{e}_{2i}(t)\big| \leq \varepsilon_{1i}, \end{cases} \\ \mathbf{B}_i(\cdot) &= \begin{cases} \beta_i\lfloor\cdot\rceil & \text{if} \quad \lfloor\cdot\rceil > \varepsilon_{2i} \\ \beta_i\varepsilon_{2i} & \text{if} \quad \lfloor\cdot\rceil \leq \varepsilon_{2i}, \qquad i = \overline{1,6} \\ \lfloor\cdot\rceil = & \big|\mathbf{e}_{2i}(t)\big|\tanh[\mathbf{e}_{2i}(t)] \end{cases} \\ \boldsymbol{\Lambda}_i(\cdot) &= \begin{cases} \bar{\lambda}_{0i}\big|\int\mathbf{e}_{2i}(t)\big|^{(\delta_{2i}-1)} & \text{if} \quad \big|\int\mathbf{e}_{2i}(t)\big| > \varepsilon_{3i} \\ \bar{\lambda}_{0i}\varepsilon_{3i}^{(\delta_{2i}-1)} & \text{if} \quad \big|\int\mathbf{e}_{2i}(t)\big| \leq \varepsilon_{3i} \end{cases}\end{aligned} \tag{17}$$

where in (17), $k_{0i}, \beta_i, \bar{\lambda}_{0i}, \delta_{1i}, \delta_{2i}, \varepsilon_{1i}, \varepsilon_{2i}$, and ε_{3i} are the positive design constants for the proposed controller's parameters.

Remark 2 : *The proposed S$^+$RISE assumes continuous state measurements, which may not be the case for real-life applications. Hence, we propose to resolve this issue by designing a new observer, as introduced in Section IV.*

B. Closed-loop Stability Analysis

To analyze the stability of the closed-loop dynamics of the proposed S$^+$RISE control law, we designed another auxiliary filter-tracking error $\mathbf{e}_a(t)$ as follows:

$$\mathbf{e}_a(t) = \dot{\mathbf{e}}_2(t) + \boldsymbol{\Lambda}(\cdot)\tanh[\mathbf{e}_2(t)] \tag{18}$$

where $\mathbf{e}_a(t)$ is the auxiliary filter-tracking error, whereas the remaining terms in (18) have been defined previously. In this stage, it is necessary to make the following remarks to highlight our contributions.

Remark 3 : *The error term* $\mathbf{e}_a(t)$ *is not used in the proposed S$^+$RISE control scheme since it depends on the inaccessible state, namely the acceleration* $\ddot{\boldsymbol{\eta}}(t)$*. Indeed, the term* $\mathbf{e}_a(t)$ *is designed to facilitate the stability analysis.*

The vehicle open-loop tracking error dynamics can be computed by multiplying (18) by $\mathbf{M}_{\boldsymbol{\eta}}^{\star}(\boldsymbol{\eta})$ as follows:

$$\mathbf{M}_{\boldsymbol{\eta}}^{\star}(\boldsymbol{\eta})\mathbf{e}_a(t) = \mathbf{M}_{\boldsymbol{\eta}}^{\star}(\boldsymbol{\eta})\Big[\dot{\mathbf{e}}_2(t) + \boldsymbol{\Lambda}(\cdot)\tanh[\mathbf{e}_2(t)]\Big] \tag{19}$$

Substituting (7) into (19) and using (13)–(14), we obtain

$$\mathbf{M}_{\boldsymbol{\eta}}^{\star}(\boldsymbol{\eta})\mathbf{e}_a(t) = \mathbf{F}_d + \mathbf{S} + \bar{\boldsymbol{\omega}}_{\boldsymbol{\eta}}^{\star}(t) - \boldsymbol{\tau}_{\boldsymbol{\eta}}^{\star}(\boldsymbol{\eta}) \tag{20}$$

where $\mathbf{F}_d = [\mathbf{M}_{\boldsymbol{\eta}}^{\star}(\boldsymbol{\eta}_d)\ddot{\boldsymbol{\eta}}_d + \mathbf{D}_{\boldsymbol{\eta}}^{\star}(\boldsymbol{\nu}_d, \boldsymbol{\eta}_d)\dot{\boldsymbol{\eta}}_d + \mathbf{g}_{\boldsymbol{\eta}}^{\star}(\boldsymbol{\eta}_d)] \in \mathbb{R}^{6\times1}$ and $\mathbf{S} = \Big[\mathbf{M}_{\boldsymbol{\eta}}^{\star}(\boldsymbol{\eta})\ddot{\boldsymbol{\eta}} + \mathbf{D}_{\boldsymbol{\eta}}^{\star}(\boldsymbol{\nu}, \boldsymbol{\eta})\dot{\boldsymbol{\eta}} + \mathbf{g}_{\boldsymbol{\eta}}^{\star}(\boldsymbol{\eta}) - \mathbf{F}_d + \mathbf{M}_{\boldsymbol{\eta}}^{\star}(\boldsymbol{\eta})[\dot{\mathbf{e}}_2(t) + \boldsymbol{\Lambda}(\cdot)\tanh[\mathbf{e}_2(t)]]\Big] \in \mathbb{R}^{6\times1}$ are auxiliary functions, $\bar{\boldsymbol{\omega}}_{\boldsymbol{\eta}}^{\star}(t) = -\boldsymbol{\omega}_{\boldsymbol{\eta}}^{\star}(t)$, $\boldsymbol{\nu}_d$ is a vector of the desired velocities, and $\boldsymbol{\nu}$ can be computed from (1).

The resulting closed-loop error system can be obtained by considering the time derivative of (20), which results in

$$\mathbf{M}^{\star}_{\boldsymbol{\eta}}(\boldsymbol{\eta})\dot{\mathbf{e}}_a(t) = -\dot{\mathbf{M}}^{\star}_{\boldsymbol{\eta}}(\boldsymbol{\eta})\mathbf{e}_a(t) + \dot{\mathbf{F}}_d + \dot{\mathbf{S}} + \dot{\bar{\boldsymbol{\omega}}}^{\star}_{\boldsymbol{\eta}}(t) - \dot{\boldsymbol{\tau}}^{\star}_{\boldsymbol{\eta}}(\boldsymbol{\eta}) \quad (21)$$

Injecting the first-time derivative of the proposed S$^+$RISE control law into (21) yields

$$\begin{aligned}\mathbf{M}^{\star}_{\boldsymbol{\eta}}(\boldsymbol{\eta})\dot{\mathbf{e}}_a(t) &= -\dot{\mathbf{M}}^{\star}_{\boldsymbol{\eta}}(\boldsymbol{\eta})\mathbf{e}_a(t) + \dot{\mathbf{F}}_d + \dot{\mathbf{S}} + \dot{\bar{\boldsymbol{\omega}}}^{\star}_{\boldsymbol{\eta}}(t) - \Big[\boldsymbol{\varphi}^{\star}(t) \\ &+ \dot{\mathbf{K}}(\cdot)\mathbf{e}_2(t) + (\mathbf{K}(\cdot)+\mathbf{I})\dot{\mathbf{e}}_2(t) + (\mathbf{k}_0+\mathbf{I})\boldsymbol{\Lambda}(\cdot)\tanh\left[\mathbf{e}_2(t)\right]\Big]\end{aligned} \quad (22)$$

where $\mathbf{k}_0 \in \mathbb{R}^{6\times 6}$ denotes a diagonal matrix with $k_{0i}, i = \overline{1,6}$ elements. By introducing $\mathbf{N}_d \in \mathbb{R}^{6\times 1}$ and $\tilde{\mathbf{N}} \in \mathbb{R}^{6\times 1}$ defined by

$$\mathbf{N}_d = \dot{\mathbf{F}}_d + \dot{\bar{\boldsymbol{\omega}}}^{\star}_{\boldsymbol{\eta}}(t) \text{ and } \tilde{\mathbf{N}} = -\frac{1}{2}\dot{\mathbf{M}}^{\star}_{\boldsymbol{\eta}}(\boldsymbol{\eta})\mathbf{e}_a(t) + \dot{\mathbf{S}} \quad (23)$$

we can rewrite (22) as

$$\begin{aligned}\mathbf{M}^{\star}_{\boldsymbol{\eta}}(\boldsymbol{\eta})\dot{\mathbf{e}}_a(t) &= -\frac{1}{2}\dot{\mathbf{M}}^{\star}_{\boldsymbol{\eta}}(\boldsymbol{\eta})\mathbf{e}_a(t) + \tilde{\mathbf{N}} + \mathbf{N}_d - \boldsymbol{\varphi}^{\star}(t) - \mathbf{e}_a(t) \\ &- \dot{\mathbf{K}}(\cdot)\mathbf{e}_2(t) - \mathbf{K}(\cdot)\dot{\mathbf{e}}_2(t) - \mathbf{k}_0\boldsymbol{\Lambda}(\cdot)\tanh\left[\mathbf{e}_2(t)\right]\end{aligned} \quad (24)$$

Note that (23) is structured such that the terms to be upper-bounded by constants can be isolated from state-dependent terms [10]. Based on this observation and the properties **P1** − **P5**, the terms $\mathbf{N}_d$ and $\tilde{\mathbf{N}}$ can be upper bounded as follows [28]:

$$\left\|\tilde{\mathbf{N}}\right\| \le \rho(\|\mathbf{r}_a\|)\|\mathbf{r}_a\|, \quad \|\mathbf{N}_d\| \le \zeta_1 \text{ and } \left\|\dot{\mathbf{N}}_d\right\| \le \zeta_2 \quad (25)$$

where $\zeta_1 \in \mathbb{R}_{>0}$ and $\zeta_2 \in \mathbb{R}_{>0}$ are positive constants and $\rho \in \mathbb{R}_{>0}$ is a strictly increasing function of $\|\mathbf{r}_a\|$. The term $\mathbf{r}_a$ is designed as follows:

$$\mathbf{r}_a = \left[\tanh^{\mathrm{T}}\left[\mathbf{e}_1(t)\right], \tanh^{\mathrm{T}}\left[\mathbf{e}_2(t)\right], \mathbf{e}_a^{\mathrm{T}}(t)\right]^{\mathrm{T}} \quad (26)$$

In the following, we state the main theorem of this analysis

Theorem 1 : The trajectory $\boldsymbol{\eta}(t)$ of an underwater vehicle whose nonlinear-coupled-uncertain dynamics are described by (7), under the proposed S$^+$RISE controller in (15), is bounded and converges uniformly asymptotically to the desired trajectory $\boldsymbol{\eta}_d(t)$, despite the influences of parametric uncertainties and external disturbances, provided that the parameters of the proposed controller are designed such that:

$$\begin{aligned}\left\|\mathbf{r}_a(0)\right\| < \rho^{-1}\left(\sqrt{\gamma(2+6K_{\min})}\right), \alpha_{\min} > \frac{1}{2}, \Lambda_{\min} > \frac{1}{2}, \\ K_{\min} > \frac{1}{2}, \text{ and } B_{\min} > \zeta_1 + \frac{1}{\Lambda_{\min}}\zeta_2\end{aligned} \quad (27)$$

where $B_{\min}, K_{\min}, \Lambda_{\min} \in \mathbb{R}_{>0}$ are obtained from the arguments $B_{\min} \le \mathbf{B}_i(\cdot) \le B_{\max}, K_{\min} \le \mathbf{K}_i(\cdot) \le K_{\max}$, and $\Lambda_{\min} \le \boldsymbol{\Lambda}_i(\cdot) \le \Lambda_{\max}$, respectively. Moreover, the terms $\mathbf{B}_i(\cdot), \mathbf{K}_i(\cdot), \boldsymbol{\Lambda}_i(\cdot)$ are designed in (17), $\boldsymbol{\alpha}$ is defined in (14), and γ is derived subsequently.

Proof of Theorem 1 : To proceed with this proof, based on the Lyapunov direct method, let us first consider the Lyapunov candidate function $V_c : \mathbb{R}^{[\dim(\mathbf{r}_a)+1]\times 1} \times \mathbb{R}_{\geqslant 0} \to \mathbb{R}_{>0}$, which is defined as follows:

$$\begin{aligned}V_c(\mathbf{z},t) = \sum_{i=1}^{6}\ln\left[\cosh\left(\mathbf{e}_{1i}\right)\right] + \sum_{i=1}^{6}\ln\left[\cosh\left(\mathbf{e}_{2i}\right)\right] + Q \\ + \frac{1}{2}{\mathbf{e}_a}^{\mathrm{T}}\mathbf{M}^{\star}_{\boldsymbol{\eta}}(\boldsymbol{\eta})\mathbf{e}_a\end{aligned} \quad (28)$$

which satisfies the following condition:

$$\begin{aligned}\frac{1}{2}\min\{1,\kappa\}\tanh^2\left[\|\mathbf{z}\|\right] = f_1(\mathbf{z}) \le V_c(\mathbf{z},t) \le f_2(\mathbf{z}) \\ = \max\left\{\frac{1}{2}\kappa(\boldsymbol{\eta}), \frac{3}{2}\right\}\|\mathbf{z}\|^2\end{aligned} \quad (29)$$

where ln represents a natural logarithmic function, cosh defines a hyperbolic cosine function, $\mathbf{z} = [\mathbf{r}_a^{\mathrm{T}}, \sqrt{Q}]^{\mathrm{T}}$, and $f_1, f_2 : \mathbb{R}^{[\dim(\mathbf{r}_a)+1]\times 1} \to \mathbb{R}_{>0}$ are strictly positive definite functions. Function $Q \in \mathbb{R}$ is positive definite, resulting from the solution of the following equation:

$$\dot{Q} = -\mathbf{e}_a^{\mathrm{T}}(t)[\mathbf{N}_d - \boldsymbol{\varphi}^{\star}(t)] \quad (30)$$

where $Q_0 = \sum_{i=1}^{6}\mathbf{B}_i(\cdot)\left|\tanh\left[\mathbf{e}_{2i}(t_0)\right]\right| - \tanh^{\mathrm{T}}\left[\mathbf{e}_2(t_0)\right]\mathbf{N}_d(t_0)$ and $\mathbf{B}_i(\cdot)$ satisfies condition (27). Furthermore, *Lemma 1* in [28] can easily be used to prove that the solution of $\dot{Q}$ is positive definite and bounded by $B_{\min}$.

The computation of the first-time derivative of the proposed Lyapunov candidate function $V_c(\mathbf{z},t)$ in (28) leads to

$$\begin{aligned}\dot{V}_c(\mathbf{z},t) = \dot{\mathbf{e}}_1^{\mathrm{T}}\tanh\left[\mathbf{e}_1\right] + \dot{\mathbf{e}}_2^{\mathrm{T}}\tanh\left[\mathbf{e}_2\right] + \dot{Q} + \dot{\mathbf{e}}_a^{\mathrm{T}}\mathbf{M}^{\star}_{\boldsymbol{\eta}}(\boldsymbol{\eta})\mathbf{e}_a \\ + \frac{1}{2}{\mathbf{e}_a}^{\mathrm{T}}\dot{\mathbf{M}}^{\star}_{\boldsymbol{\eta}}(\boldsymbol{\eta})\mathbf{e}_a\end{aligned} \quad (31)$$

Substituting the closed-loop error dynamics (24) into (31) and using (14) and (18), we derive

$$\begin{aligned}\dot{V}_c(\mathbf{z},t) = \mathbf{e}_2^{\mathrm{T}}\tanh\left[\mathbf{e}_1\right] - \tanh^{\mathrm{T}}\left[\mathbf{e}_1\right]\boldsymbol{\alpha}\tanh\left[\mathbf{e}_1\right] \\ + {\mathbf{e}_a}^{\mathrm{T}}\tanh\left[\mathbf{e}_2\right] - \tanh^{\mathrm{T}}\left[\mathbf{e}_2\right]\boldsymbol{\Lambda}(\cdot)\tanh\left[\mathbf{e}_2\right] - {\mathbf{e}_a}^{\mathrm{T}}\mathbf{e}_a \\ + {\mathbf{e}_a}^{\mathrm{T}}\tilde{\mathbf{N}} - {\mathbf{e}_a}^{\mathrm{T}}\dot{\mathbf{K}}(\cdot)\mathbf{e}_2 - {\mathbf{e}_a}^{\mathrm{T}}\Big[\mathbf{K}(\cdot)\dot{\mathbf{e}}_2 + \mathbf{k}_0\boldsymbol{\Lambda}(\cdot)\tanh\left[\mathbf{e}_2\right]\Big]\end{aligned} \quad (32)$$

In fact, $\dot{V}_c(\mathbf{z},t)$ in (32) can be bounded, such that

$$\begin{aligned}\dot{V}_c(\mathbf{z},t) \le \frac{\|\mathbf{e}_2\|^2}{2} + \frac{\left\|\tanh\left[\mathbf{e}_1\right]\right\|^2}{2} - \alpha_{\min}\left\|\tanh\left[\mathbf{e}_1\right]\right\|^2 + \frac{\|\mathbf{e}_a\|^2}{2} \\ + \frac{\left\|\tanh\left[\mathbf{e}_2\right]\right\|^2}{2} - \Lambda_{\min}\left\|\tanh\left[\mathbf{e}_2\right]\right\|^2 + \|\mathbf{e}_a\|\rho(\|\mathbf{r}_a\|)\|\mathbf{r}_a\| \\ - \frac{K_{\min}}{2}\|\mathbf{e}_a\|^2 - \frac{K_{\min}}{2}\|\mathbf{e}_2\|^2 - \|\mathbf{e}_a\|^2 - K_{\min}\|\mathbf{e}_a\|^2\end{aligned} \quad (33)$$

which can be rewritten as

$$\begin{aligned}\dot{V}_c(\mathbf{z},t) \le -(\alpha_{\min} - \frac{1}{2})\left\|\tanh\left[\mathbf{e}_1\right]\right\|^2 - (\Lambda_{\min} - \frac{1}{2}) \\ \times\left\|\tanh\left[\mathbf{e}_2\right]\right\|^2 - (K_{\min} - \frac{1}{2})\|\mathbf{e}_2\|^2 + \frac{\rho^2(\|\mathbf{r}_a\|)\|\mathbf{r}_a\|^2}{2(1+3K_{\min})}\end{aligned} \quad (34)$$

As long as (27) holds, $\dot{V}_c(\mathbf{z},t)$ in (34) can be further simplified and upper-bounded as follows:

$$\dot{V}_c(\mathbf{z},t) \le -\left[\gamma - \frac{\rho^2(\|\mathbf{r}_a\|)}{2(1+3K_{\min})}\right]\|\mathbf{r}_a\|^2 \quad (35)$$

This article has been accepted for publication in IEEE Transactions on Control Systems Technology. This is the author's version which has not been fully edited and content may change prior to final publication. Citation information: DOI 10.1109/TCST.2022.3224321

where $\gamma = \min\{(\alpha_{\min} - \frac{1}{2}), (\Lambda_{\min} - \frac{1}{2}), (K_{\min} - \frac{1}{2})\}$ and $\|\mathbf{r}_a\| < \rho^{-1}\left(\sqrt{\gamma(2+6K_{\min})}\right)$.
From (35), we can easily observe that $\dot{V}_c(\mathbf{z},t)$ is bounded by a negative semi-definite function. Based on the fact that $V_c(\mathbf{z},t)$ is a continuous and positive definite function, satisfying (29), we can conclude that $\|\mathbf{r}_a\|^2$ is bounded and remains within a compact set $\mathcal{S}_{\mathcal{D}} = \left\{\mathbf{z} \in \mathcal{D} \mid \rho(\sqrt{f_2(\mathbf{z})}) < \sqrt{\gamma(2+6K_{\min})}\right\}$, where $\mathcal{D} = \left\{\mathbf{z} \in \mathbb{R}^{[\dim(\mathbf{r}_a)+1]\times 1} \mid \|\mathbf{z}\| \leq \inf\left(\rho^{-1}[\sqrt{\gamma(2+6K_{\min})}, \infty)\right)\right\}$. This implies that $\|\mathbf{r}_a\| \to 0$, $\forall \mathbf{z}(0) \in \mathcal{S}_{\mathcal{D}}$, which guarantees a semiglobal asymptotic convergence of the tracking error to zero. The value of $K_{\min}$ can be increased to make $\mathcal{S}_{\mathcal{D}}$ arbitrarily large and accommodate a large $\mathbf{z}(0)$. At this stage, it is necessary to consider the following.
Remark 4 : *In some real-time applications increasing* $K_{\min}$, *so that* $\mathcal{S}_{\mathcal{D}}$ *can include large* $\mathbf{z}(0)$, *as well as large disturbances, may lead to control signals beyond the admissible limits of the actuators. Hence, the semi-global result may be affected by the high impact of unbounded perturbations; however, the local result can still be maintained.*

IV. PROPOSED OBSERVER DESIGN AND ITS PERFORMANCE ANALYSIS

A. Observer Design

This section presents and discusses the design of the proposed Continuous Discrete Observer (CDO). This observer is an extension of the one developed in [29]. Even though the observer proposed in [29] was designed to estimate the lost measurements between sensor sampling periods, asynchronous multirate sensor measurements have not been considered. In practice, physical systems are typically equipped with several sensors that operate at different sampling frequencies. Designing an observer for such systems without considering the different operating frequencies of their sensors may lead to instability in the overall closed-loop dynamics. This issue may become more complex in high-precision applications, particularly at low sensor sampling frequencies.

To address this sampling issue, we propose a CDO that works in tandem with the S$^+$RISE control scheme introduced in the previous section. The goal of the CDO is to provide continuous state and disturbance estimations to the proposed controller. It is worth noting that, when new measurements are acquired by the sensors, the proposed observer corrects the corresponding estimates. In addition to being equipped with inter-sample predictors to address the issue of asynchronous multirate sensors, the proposed CDO uses optimal gains by exploiting the well-known linear matrix inequalities (LMI) technique. These gains improve the observer design proposed by [29], where the gains are tuned based on a trial-and-error approach. Furthermore, the observers in [29] and [24] considered only the case of uniform single-rate sensor measurements. In fact, we propose to incorporate a correction term in the predictor design to enhance and guarantee the exponential convergence of the proposed CDO estimation error towards zero. In contrast to neurodynamics and MPC-based techniques, the proposed CDO is designed as a computationally lightweight scheme and validated through real-time experiments on a low-cost underwater vehicle. *It is worth noting that the vehicle used in this work is equipped with sensors having different sampling frequencies, as reported in Table I.* The measurable state of this vehicle is accessible by the proposed observer through the depth and IMU sensors' discrete-time measurement vector $\mathbf{y}(t_k^1, \cdots, t_k^{\bar{s}}) \in \mathbb{R}^{\bar{s}\times 1}$with $\bar{s}, k \in \mathbb{N}$. Hence, the vehicle dynamics in (11) can be rewritten as follows:

$$\begin{cases} \dot{\boldsymbol{\chi}}(t) = \tilde{\mathbf{A}}\boldsymbol{\chi}(t) + \tilde{\mathbf{B}}_{\boldsymbol{\chi}(t)}\mathbf{u}(t) + \tilde{\mathbf{D}}\boldsymbol{\delta}^\star(t) \\ \mathbf{y}(t_k^1, \cdots, t_k^{\bar{s}}) = \tilde{\mathbf{C}}\boldsymbol{\chi}(t_k^1, \cdots, t_k^{\bar{s}}) \end{cases} \tag{36}$$

where $\bar{s}, k \in \mathbb{N}$ denote the number of sensors and their sampling time, respectively. The sensor sampling periods are denoted as $\{[t_k^1\ t_{k+1}^1], [t_k^2\ t_{k+1}^2], \cdots, [t_k^{\bar{s}}\ t_{k+1}^{\bar{s}}]\}$ and $\tilde{\mathbf{C}} \in \mathbb{R}^{\bar{s}\times \dim(\boldsymbol{\chi})}$ denotes the output matrix. To address the effects of external disturbances and parametric uncertainties in the structure of the proposed CDO design, we rewrite (36) in an extended state-space form as follows:

$$\begin{cases} \dot{\bar{\boldsymbol{\chi}}}(t) = \bar{\mathbf{A}}\bar{\boldsymbol{\chi}} + \bar{\mathbf{B}}_{\bar{\boldsymbol{\chi}}(t)}\mathbf{u}(t) + \bar{\mathbf{D}}\bar{\boldsymbol{\delta}}(t) \\ \bar{\mathbf{y}}(t_k^1, \cdots, t_k^{\bar{s}}) = \bar{\mathbf{C}}\bar{\boldsymbol{\chi}}(t_k^1, \cdots, t_k^{\bar{s}}) \end{cases} \tag{37}$$

where $\bar{\boldsymbol{\chi}}(t) = [\boldsymbol{\chi}(t)^{\mathrm{T}}\ \ \boldsymbol{\delta}^\star(t)^{\mathrm{T}}]^{\mathrm{T}}$, $\bar{\mathbf{A}} = \begin{bmatrix} \tilde{\mathbf{A}} & \tilde{\mathbf{D}} \\ \mathbf{0}_{6\times 12} & \mathbf{0}_{6\times 6} \end{bmatrix}$, $\bar{\boldsymbol{\delta}}(t) = \boldsymbol{\delta}^\star(t)$, $\bar{\mathbf{B}} = \begin{bmatrix} \tilde{\mathbf{B}} & \mathbf{0}_{6\times 6} \end{bmatrix}^{\mathrm{T}}$, $\bar{\mathbf{D}} = \begin{bmatrix} \mathbf{0}_{6\times 6} & \tilde{\mathbf{D}} \end{bmatrix}^{\mathrm{T}}$, and $\bar{\mathbf{C}} = \begin{bmatrix} \tilde{\mathbf{C}} & \mathbf{0}_{6\times 6} \end{bmatrix}$.
Even though the proposed S$^+$RISE is a model-free scheme, in practice, the proposed CDO requires an estimate of the inertia matrix $\mathbf{M}_{\boldsymbol{\eta}}^\star(\boldsymbol{\eta})$ (see [30] for more details on its numerical estimation).
Remark 5 : *The term* $\boldsymbol{\delta}^\star(t)$ *in (36) is also assumed to be bounded based on assumption* **A1** *and properties* **P1** $-$ **P4**, *which implies that* $\left\|\boldsymbol{\delta}^\star(t)\right\| \leq L_1$ *and* $\left\|\dot{\boldsymbol{\delta}}^\star(t)\right\| \leq L_2$. where $L_1 \in \mathbb{R}_{>0}$ and $L_2 \in \mathbb{R}_{>0}$ denote positive constants.
Finally, the proposed CDO for underwater vehicle dynamics in (37) is designed as follows:

$$\begin{cases} \dot{\hat{\bar{\boldsymbol{\chi}}}}(t) = \bar{\mathbf{A}}\hat{\bar{\boldsymbol{\chi}}}(t) + \bar{\mathbf{B}}^\star_{\hat{\boldsymbol{\chi}}(t)}\mathbf{u}(t) + \boldsymbol{\Delta}_\theta \mathbf{K}^\star[\mathbf{w}(t) - \bar{\mathbf{C}}\hat{\bar{\boldsymbol{\chi}}}(t)] \\ \dot{\mathbf{w}}(t) = \bar{\mathbf{C}}[\bar{\mathbf{A}}\hat{\bar{\boldsymbol{\chi}}}(t) + \bar{\mathbf{B}}^\star_{\hat{\boldsymbol{\chi}}(t)}\mathbf{u}(t)] + \mathbf{K}_{\mathbf{w}}[\mathbf{w}(t) - \bar{\mathbf{C}}\hat{\bar{\boldsymbol{\chi}}}(t)] \\ \mathbf{w}(t_k^1, \cdots, t_k^{\bar{s}}) = \bar{\mathbf{y}}(t_k^1, \cdots, t_k^{\bar{s}}),\ t \in [t_k^{\bar{s}}\ t_{k+1}^{\bar{s}}) \end{cases} \tag{38}$$

where $\hat{\bar{\boldsymbol{\chi}}}(t)$ is the vector of the extended state estimates, $\boldsymbol{\Delta}_\theta$= $diag\{\theta, \theta^2, \cdots, \theta^{[\dim(\bar{\boldsymbol{\chi}})]}\}$, where θ denotes the high-gain parameter, $\bar{\mathbf{B}}^\star_{\hat{\boldsymbol{\chi}}(t)}$ is the nominal value of $\bar{\mathbf{B}}_{\bar{\boldsymbol{\chi}}(t)}$, $\mathbf{K}^\star \in \mathbb{R}^{\dim(\bar{\boldsymbol{\chi}})\times \bar{s}}$ is the observer gain designed such that $[\bar{\mathbf{A}} - \mathbf{K}^\star\bar{\mathbf{C}}]$ is Hurwitz, $\mathbf{K}_{\mathbf{w}}$ defines the predictor design gain, and $\mathbf{w}(t) \in \mathbb{R}^{\bar{s}\times 1}$ is the vector of the continuous time estimation of $\bar{\mathbf{y}}(t_k^1, \cdots, t_k^{\bar{s}})$, whose elements are updated at each $t \in (t_k^1, \cdots, t_k^{\bar{s}})$. The main motivation for integrating term $\mathbf{w}(t)$ is to dealt with the significant effect caused by the multirate sampling of the system's output acquired through multiple sensors. Furthermore, the term $\mathbf{w}(t)$ mitigates the instability and divergence behavior of the dynamic system owing to the low sampling rate.
It is worth noting the following.

1) The proposed S$^+$RISE control input $\boldsymbol{\tau}$ is globally bounded by design;

2) The origin of the closed-loop dynamics resulting from (7) and the proposed S$^+$RISE control law is asymptotically stable, having $\mathbb{S}_{\mathfrak{D}}$ as its region of attraction.

B. Performance Recovery Analysis

To demonstrate how the resulting closed-loop error dynamics of (37)–(38) recover the performance of the closed-loop error dynamics under the proposed S$^+$RISE state, feedback control in (21), we first check the exponential convergence of the unperturbed fast closed-loop system, as follows:

1) Convergence analysis of the unperturbed system: To verify the exponential convergence of the unperturbed resulting closed-loop dynamics of our underwater vehicle with the proposed observation-based control scheme CDO-S$^+$RISE to the origin, we state the main result of the study as follows:

Theorem 2 : *Consider an underwater vehicle whose dynamics are given in (36) and candidate observer (38). If there exist symmetric positive definite matrices* $\mathbf{P}_k$*,* $\mathbf{P}$*,* $\mathbf{P}_1$*,* $\mathbf{P}_2$*,* $\mathbf{P}_3$*,* $\mathbf{P}_4$*,* $\mathbf{R}$*,* $\mathbf{H}$*, and the observer gain* $\mathbf{K}^\star$*, as well as the predictor gain* $\mathbf{K_w}$*, such that the LMI conditions (39)-(41) hold, then (38) is a sampled-data observer for the extended state dynamics (37). Moreover, for a given sampling period h that satisfies* $h = \sqrt{\|\mathbf{H}\mathbf{R}^{-1}\|}$*, the trajectories of the state estimation error dynamics converge exponentially towards the origin, as long as the observer high-gain parameter* θ *is designed to be sufficiently large.*

$$(\mathbf{K_w} - \bar{\mathbf{C}}\bar{\mathbf{K}}^\star)^{\mathrm{T}}\mathbf{P}_k + \mathbf{P}_k(\mathbf{K_w} - \bar{\mathbf{C}}\bar{\mathbf{K}}^\star) \leq 0 \tag{39}$$

$$\boldsymbol{\Phi}_1 = \begin{bmatrix} (\bar{\mathbf{A}} - \mathbf{K}^\star\bar{\mathbf{C}})^{\mathrm{T}}\mathbf{P} + \mathbf{P}(\bar{\mathbf{A}} - \mathbf{K}^\star\bar{\mathbf{C}}) & \mathbf{P}\mathbf{K}^\star\bar{\mathbf{C}} \\ * & -\mathbf{S} \end{bmatrix} \leq -\lambda \mathbf{I}_n \tag{40}$$

$$\boldsymbol{\Phi}_2 = \begin{bmatrix} \boldsymbol{\Phi}_{11} & \boldsymbol{\Phi}_{12} & \boldsymbol{\Phi}_{13} & \mathbf{R} \\ * & \boldsymbol{\Phi}_{22} & \boldsymbol{\Phi}_{23} & \mathbf{0} \\ * & * & \boldsymbol{\Phi}_{33} & \mathbf{0} \\ * & * & * & -\mathbf{R} \end{bmatrix} \leq 0 \tag{41}$$

where $\bar{\mathbf{K}}^\star = \boldsymbol{\Delta}_\theta\mathbf{K}^\star, \boldsymbol{\Phi}_{11} = \lambda\mathbf{S} + \mathbf{K_w}\mathbf{P}_2 + \mathbf{P}_2^{\mathrm{T}}\bar{\mathbf{K}}_\mathbf{w} - \mathbf{R}$, $\boldsymbol{\Phi}_{12} = \mathbf{P}_2^{\mathrm{T}}\theta\mathbf{A}_1 - \mathbf{P}_2^{\mathrm{T}}\bar{\mathbf{K}}_\mathbf{w}$, $\boldsymbol{\Phi}_{13} = \mathbf{P}_1^{\mathrm{T}} - \mathbf{P}_2 + \bar{\mathbf{K}}_\mathbf{w}^{\mathrm{T}}\mathbf{P}_3$, $\boldsymbol{\Phi}_{22} = -\mathbf{P}_4^{\mathrm{T}}\theta\mathbf{A}_1 - \mathbf{P}_4^{\mathrm{T}}\bar{\mathbf{K}}_\mathbf{w}$, $\boldsymbol{\Phi}_{23} = \mathbf{P}_4 + \theta\mathbf{A}_1^{\mathrm{T}}\mathbf{P}_3 - \bar{\mathbf{K}}_\mathbf{w}^{\mathrm{T}}\mathbf{P}_3$, $\boldsymbol{\Phi}_{33} = -\mathbf{P}_3 - \mathbf{P}_3^{\mathrm{T}} + \mathbf{H}$, $\bar{\mathbf{K}}_\mathbf{w}, \mathbf{A}_1, \mathbf{S}$ *are defined in the subsequent proof,* λ *is a positive constant, and* $\mathbf{I}_n$ *is an Identity matrix.*

Proof of Theorem 2: First, we define the following estimation errors.

$$\begin{cases} \mathbf{e}_x &= \bar{\boldsymbol{\chi}}(t) - \hat{\bar{\boldsymbol{\chi}}}(t) \\ \mathbf{e}_y &= \bar{\mathbf{C}}\bar{\boldsymbol{\chi}}(t) - \mathbf{w}(t) \end{cases} \tag{42}$$

Before proving the exponential convergence of $\hat{\bar{\boldsymbol{\chi}}}(t)$ to $\bar{\boldsymbol{\chi}}(t)$, the stable behavior of the output prediction dynamics $\dot{\mathbf{w}}(t)$ in (38) must be ensured when measurements are not available. Using (42) and $\dot{\mathbf{w}}(t)$ dynamics, the output prediction error dynamics can be derived as follows:

$$\dot{\mathbf{e}}_y - \bar{\mathbf{C}}\dot{\mathbf{e}}_x = (\mathbf{K_w} - \bar{\mathbf{C}}\bar{\mathbf{K}})(\mathbf{e}_y - \bar{\mathbf{C}}\mathbf{e}_x) \tag{43}$$

Now, consider the following Lyapunov function candidate, V_o:

$$V_o = [\mathbf{e}_y - \bar{\mathbf{C}}\mathbf{e}_x]^{\mathrm{T}}\mathbf{P}_k[\mathbf{e}_y - \bar{\mathbf{C}}\mathbf{e}_x] \tag{44}$$

where $\mathbf{P}_k, \mathbf{e}_y, \mathbf{e}_x$, and $\bar{\mathbf{C}}$ have been defined previously, and V_o satisfies $\lambda_{\min}(\mathbf{P}_k)\left\|[\mathbf{e}_y - \bar{\mathbf{C}}\mathbf{e}_x]\right\|^2 \leq V_o \leq \lambda_{\max}(\mathbf{P}_k)\left\|[\mathbf{e}_y - \bar{\mathbf{C}}\mathbf{e}_x]\right\|^2$, with $\lambda_{\min}([\cdot])$ and $\lambda_{\max}([\cdot])$ as the minimum and maximum eigenvalues of the matrix $[\cdot]$, respectively.

Differentiating (44) and (43) yields LMI condition (39). If this condition holds, stable behavior of $\dot{\mathbf{w}}(t)$ dynamics in (38) is guaranteed.

Let us analyze the exponential convergence of $\hat{\bar{\boldsymbol{\chi}}}(t)$ to $\bar{\boldsymbol{\chi}}(t)$. Combining (37)–(38) and (42), we derive the following:

$$\begin{aligned} \dot{\mathbf{e}}_x(t) &= (\bar{\mathbf{A}} - \boldsymbol{\Delta}_\theta\mathbf{K}^\star\bar{\mathbf{C}})\mathbf{e}_x(t) + \boldsymbol{\Phi}(\cdot)\mathbf{u} + \bar{\mathbf{D}}\bar{\boldsymbol{\delta}} + \boldsymbol{\Delta}_\theta\mathbf{K}^\star\mathbf{e}_y(t) \\ \dot{\mathbf{e}}_y(t) &= (\bar{\mathbf{C}}\bar{\mathbf{A}} - \mathbf{K_w}\bar{\mathbf{C}})\mathbf{e}_x(t) + \mathbf{K_w}\mathbf{e}_y(t) \end{aligned} \tag{45}$$

where the uncertainty $\boldsymbol{\Phi}(\cdot) = \bar{\mathbf{B}}_{\bar{\boldsymbol{\chi}}(t)} - \bar{\mathbf{B}}^\star_{\hat{\boldsymbol{\chi}}(t)}$ (a nonlinear function satisfying conditions (i)–(ii) in Assumption 1 in [31]). We note that $\bar{\mathbf{C}}\bar{\mathbf{B}} = 0$. At this stage, the following errors were considered: $\boldsymbol{\varepsilon}_{x(t)} = \boldsymbol{\Delta}_\theta^{-1}\mathbf{e}_x$ and $\boldsymbol{\varepsilon}_{y(t)} = \boldsymbol{\Delta}_\theta^{-1}\bar{\mathbf{C}}^{\mathrm{T}}\mathbf{e}_y$. Hence, (45) can be rewritten as

$$\begin{aligned} \dot{\boldsymbol{\varepsilon}}_{x(t)} &= \boldsymbol{\Delta}_\theta^{-1}(\bar{\mathbf{A}} - \boldsymbol{\Delta}_\theta\mathbf{K}^\star\bar{\mathbf{C}})\boldsymbol{\Delta}_\theta\boldsymbol{\varepsilon}_{x(t)} + \boldsymbol{\Delta}_\theta^{-1}\boldsymbol{\Delta}_\theta\mathbf{K}^\star\bar{\mathbf{C}}\boldsymbol{\Delta}_\theta\boldsymbol{\varepsilon}_{y(t)} \\ &\quad + \boldsymbol{\Delta}_\theta^{-1}\boldsymbol{\Phi}(\cdot)\mathbf{u} + \boldsymbol{\Delta}_\theta^{-1}\bar{\mathbf{D}}\bar{\boldsymbol{\delta}} \\ \dot{\boldsymbol{\varepsilon}}_{y(t)} &= \theta\mathbf{A}_1\boldsymbol{\varepsilon}_{x(t)} - \bar{\mathbf{K}}_\mathbf{w}\boldsymbol{\varepsilon}_{x(t)} + \bar{\mathbf{K}}_\mathbf{w}\boldsymbol{\varepsilon}_{y(t)} \end{aligned} \tag{46}$$

where $\mathbf{A}_1 = \bar{\mathbf{C}}^{\mathrm{T}}\bar{\mathbf{C}}\bar{\mathbf{A}}$ and $\bar{\mathbf{K}}_\mathbf{w} = \bar{\mathbf{C}}^{\mathrm{T}}\mathbf{K_w}\bar{\mathbf{C}}$.

From (46), as the high-gain parameter θ increases, the elements of the matrix $\boldsymbol{\Delta}_\theta^{-1}$ approach 0 (i.e., $\boldsymbol{\Delta}_\theta^{-1} \to 0$), thus suppressing the negative effect of $\bar{\boldsymbol{\delta}}$ term and also making the proposed CDO dynamics faster. Accordingly, (46) can be simplified and rewritten as

$$\begin{aligned} \dot{\boldsymbol{\varepsilon}}_{x(t)} &= \boldsymbol{\Delta}_\theta^{-1}(\bar{\mathbf{A}} - \boldsymbol{\Delta}_\theta\mathbf{K}^\star\bar{\mathbf{C}})\boldsymbol{\Delta}_\theta\boldsymbol{\varepsilon}_{x(t)} + \boldsymbol{\Delta}_\theta^{-1}\boldsymbol{\Delta}_\theta\mathbf{K}^\star\bar{\mathbf{C}}\boldsymbol{\Delta}_\theta\boldsymbol{\varepsilon}_{y(t)} \\ \dot{\boldsymbol{\varepsilon}}_{y(t)} &= \theta\mathbf{A}_1\boldsymbol{\varepsilon}_{x(t)} - \bar{\mathbf{K}}_\mathbf{w}\boldsymbol{\varepsilon}_{x(t)} + \bar{\mathbf{K}}_\mathbf{w}\boldsymbol{\varepsilon}_{y(t)} \end{aligned} \tag{47}$$

Formulating the remaining LMI conditions in Theorem 2 guarantees the exponential convergence of the estimation error dynamics to zero (i.e., $\hat{\bar{\boldsymbol{\chi}}}(t) = \bar{\boldsymbol{\chi}}(t)$). Let us consider the following Lyapunov–Krasovskii functional.

$$V_{o1} = \boldsymbol{\varepsilon}^{\mathrm{T}}_{x(t)}\mathbf{P}\boldsymbol{\varepsilon}_{x(t)} + \boldsymbol{\varepsilon}^{\mathrm{T}}_{y(t)}\mathbf{P}_1\boldsymbol{\varepsilon}_{y(t)} + h\int_{-h}^{0}\int_{t+r}^{t}\dot{\boldsymbol{\varepsilon}}^{\mathrm{T}}_{y(s)}\mathbf{R}\dot{\boldsymbol{\varepsilon}}_{y(s)}dsdr \tag{48}$$

It is worth noting that the sampled dynamics of an underwater vehicle can be modelled as a time-delay system (TDS), which is why a Lyapunov–Krasovskii functional is proposed to prove convergence [32]. Even though the Lyapunov–Razumikhin function may be considered as a simple tool for TDSs stability study, the Lyapunov–Krasovskii functional is a natural generalization of the Lyapunov direct method. The first time derivative of the Lyapunov–Krasovskii functional candidate in (48) leads to

$$\begin{aligned} \dot{V}_{o1} &= 2\boldsymbol{\varepsilon}^{\mathrm{T}}_{x(t)}\mathbf{P}\boldsymbol{\Delta}_\theta^{-1}\left[(\bar{\mathbf{A}} - \boldsymbol{\Delta}_\theta\mathbf{K}^\star\bar{\mathbf{C}})\boldsymbol{\Delta}_\theta\boldsymbol{\varepsilon}_{x(t)} + \boldsymbol{\Delta}_\theta\mathbf{K}^\star\bar{\mathbf{C}}\boldsymbol{\Delta}_\theta\boldsymbol{\varepsilon}_{y(t)}\right] \\ &\quad + 2\boldsymbol{\varepsilon}^{\mathrm{T}}_{y(t)}\mathbf{P}_1\dot{\boldsymbol{\varepsilon}}_{y(t)} + h^2\dot{\boldsymbol{\varepsilon}}^{\mathrm{T}}_{y(t)}\mathbf{R}\dot{\boldsymbol{\varepsilon}}_{y(t)} - h\int_{t-h}^{t}\dot{\boldsymbol{\varepsilon}}^{\mathrm{T}}_{y(s)}\mathbf{R}\dot{\boldsymbol{\varepsilon}}_{y(s)}ds \end{aligned} \tag{49}$$

This article has been accepted for publication in IEEE Transactions on Control Systems Technology. This is the author's version which has not been fully edited and content may change prior to final publication. Citation information: DOI 10.1109/TCST.2022.3224321

Thus, (49) can be rewritten as follows:

$$\begin{aligned}\dot{V}_{o1} &= 2\boldsymbol{\varepsilon}_{x(t)}^{\mathrm{T}}\mathbf{P}\boldsymbol{\Delta}_{\theta}^{-1}[(\bar{\mathbf{A}}\boldsymbol{\Delta}_{\theta}\mathbf{K}^{\star}\bar{\mathbf{C}})\Delta\boldsymbol{\varepsilon}_{x(t)}+\boldsymbol{\Delta}_{\theta}\mathbf{K}^{\star}\bar{\mathbf{C}}\boldsymbol{\Delta}_{\theta}\boldsymbol{\varepsilon}_{y(t)}] \\ &+2[\boldsymbol{\varepsilon}_{y(t)}^{\mathrm{T}}\mathbf{P}_2^{\mathrm{T}}+\dot{\boldsymbol{\varepsilon}}_{y(t)}^{\mathrm{T}}\mathbf{P}_3^{\mathrm{T}}+\boldsymbol{\varepsilon}_{y(t)}^{\mathrm{T}}\mathbf{P}_4][-\dot{\boldsymbol{\varepsilon}}_{y(t)} \\ &+\theta\mathbf{A}_1\boldsymbol{\varepsilon}_{x(t)}-\bar{\mathbf{K}}_{\mathbf{w}}\boldsymbol{\varepsilon}_{x(t)}+\bar{\mathbf{K}}_{\mathbf{w}}\boldsymbol{\varepsilon}_{y(t)}] \\ &-h\int_{t-h}^{t}\dot{\boldsymbol{\varepsilon}}_{y(s)}^{\mathrm{T}}\mathbf{R}\dot{\boldsymbol{\varepsilon}}_{y(s)}ds+2\boldsymbol{\varepsilon}_{y(t)}^{\mathrm{T}}\mathbf{P}_1\dot{\boldsymbol{\varepsilon}}_{y(t)}+\theta\boldsymbol{\varepsilon}_{y(t)}^{\mathrm{T}}\mathbf{S}\boldsymbol{\varepsilon}_{y(t)} \\ &-\theta\boldsymbol{\varepsilon}_{y(t)}^{\mathrm{T}}\mathbf{S}\boldsymbol{\varepsilon}_{y(t)}+h^2\dot{\boldsymbol{\varepsilon}}_{y(t)}^{\mathrm{T}}\mathbf{R}\dot{\boldsymbol{\varepsilon}}_{y(t)}\end{aligned} \tag{50}$$

where $-\dot{\boldsymbol{\varepsilon}}_{y(t)}+\theta\mathbf{A}_1\boldsymbol{\varepsilon}_{x(t)}-\bar{\mathbf{K}}_{\mathbf{w}}\boldsymbol{\varepsilon}_{x(t)}+\bar{\mathbf{K}}_{\mathbf{w}}\boldsymbol{\varepsilon}_{y(t)}=0$ and $\mathbf{S}$ is a positive definite matrix. Based on Jensen's inequality [33], the integral term in (50) can be expressed as follows:

$$\begin{aligned}-h\int_{t-h}^{t}\dot{\boldsymbol{\varepsilon}}_{y(s)}^{\mathrm{T}}\mathbf{R}\dot{\boldsymbol{\varepsilon}}_{y(s)}ds &\le -\int_{t-h}^{t}\dot{\boldsymbol{\varepsilon}}_{y(s)}^{\mathrm{T}}ds\mathbf{R}\int_{t-h}^{t}\dot{\boldsymbol{\varepsilon}}_{y(s)}ds \\ &= -[\boldsymbol{\varepsilon}_{y(t)}-\boldsymbol{\varepsilon}_{y(t-h)}]^{\mathrm{T}}\mathbf{R}[\boldsymbol{\varepsilon}_{y(t)}-\boldsymbol{\varepsilon}_{y(t-h)}]\end{aligned} \tag{51}$$

Substituting (51) into (50) yields:

$$\begin{aligned}\dot{V}_{o1} &\le \theta[2\boldsymbol{\varepsilon}_{x(t)}^{\mathrm{T}}\mathbf{P}(\bar{\mathbf{A}}-\mathbf{K}^{\star}\bar{\mathbf{C}})\boldsymbol{\varepsilon}_{x(t)}+2\boldsymbol{\varepsilon}_{x(t)}^{\mathrm{T}}\mathbf{P}\mathbf{K}^{\star}\bar{\mathbf{C}}\boldsymbol{\varepsilon}_{y(t)} \\ &-\boldsymbol{\varepsilon}_{y(t)}^{\mathrm{T}}\mathbf{S}\boldsymbol{\varepsilon}_{y(t)}]+2[\boldsymbol{\varepsilon}_{y(t)}^{\mathrm{T}}\mathbf{P}_2^{\mathrm{T}}+\dot{\boldsymbol{\varepsilon}}_{y(t)}^{\mathrm{T}}\mathbf{P}_3^{\mathrm{T}}+\boldsymbol{\varepsilon}_{y(t)}^{\mathrm{T}}\mathbf{P}_4][-\dot{\boldsymbol{\varepsilon}}_{y(t)} \\ &+\theta\mathbf{A}_1\boldsymbol{\varepsilon}_{x(t)}-\bar{\mathbf{K}}_{\mathbf{w}}\boldsymbol{\varepsilon}_{x(t)}+\bar{\mathbf{K}}_{\mathbf{w}}\boldsymbol{\varepsilon}_{y(t)}] \\ &+h^2\dot{\boldsymbol{\varepsilon}}_{y(t)}^{\mathrm{T}}\mathbf{R}\dot{\boldsymbol{\varepsilon}}_{y(t)}-[\boldsymbol{\varepsilon}_{y(t)}-\boldsymbol{\varepsilon}_{y(t-h)}]^{\mathrm{T}}\mathbf{R}[\boldsymbol{\varepsilon}_{y(t)}-\boldsymbol{\varepsilon}_{y(t-h)}] \\ &+2\boldsymbol{\varepsilon}_{y(t)}^{\mathrm{T}}\mathbf{P}_1\dot{\boldsymbol{\varepsilon}}_{y(t)}+\theta\boldsymbol{\varepsilon}_{y(t)}^{\mathrm{T}}\mathbf{S}\boldsymbol{\varepsilon}_{y(t)}\end{aligned} \tag{52}$$

Now, by introducing two vectors $\overline{\boldsymbol{\eta}}_1=[\boldsymbol{\varepsilon}_{x(t)},\boldsymbol{\varepsilon}_{y(t)}]^{\mathrm{T}}$ and $\overline{\boldsymbol{\eta}}_2=[\boldsymbol{\varepsilon}_{y(t)},\boldsymbol{\varepsilon}_{x(t)},\dot{\boldsymbol{\varepsilon}}_{y(t)},\boldsymbol{\varepsilon}_{y(t-h)}]^{\mathrm{T}}$, we can express the terms $\overline{\boldsymbol{\eta}}_1^{\mathrm{T}}\boldsymbol{\Phi}_1\overline{\boldsymbol{\eta}}_1$ and $\overline{\boldsymbol{\eta}}_2^{\mathrm{T}}\boldsymbol{\Phi}_2\overline{\boldsymbol{\eta}}_2$ as $2\boldsymbol{\varepsilon}_{x(t)}^{\mathrm{T}}\mathbf{P}(\bar{\mathbf{A}}-\mathbf{K}^{\star}\bar{\mathbf{C}})\boldsymbol{\varepsilon}_{x(t)}+2\boldsymbol{\varepsilon}_{x(t)}^{\mathrm{T}}\mathbf{P}\mathbf{K}^{\star}\bar{\mathbf{C}}\boldsymbol{\varepsilon}_{y(t)}-\boldsymbol{\varepsilon}_{y(t)}^{\mathrm{T}}\mathbf{S}\boldsymbol{\varepsilon}_{y(t)}$ and $2[\boldsymbol{\varepsilon}_{y(t)}^{\mathrm{T}}\mathbf{P}_2^{\mathrm{T}}+\dot{\boldsymbol{\varepsilon}}_{y(t)}^{\mathrm{T}}\mathbf{P}_3^{\mathrm{T}}+\boldsymbol{\varepsilon}_{y(t)}^{\mathrm{T}}\mathbf{P}_4][-\dot{\boldsymbol{\varepsilon}}_{y(t)}+\theta\mathbf{A}_1\boldsymbol{\varepsilon}_{x(t)}-\bar{\mathbf{K}}_{\mathbf{w}}\boldsymbol{\varepsilon}_{x(t)}+\bar{\mathbf{K}}_{\mathbf{w}}\boldsymbol{\varepsilon}_{y(t)}]+h^2\dot{\boldsymbol{\varepsilon}}_{y(t)}^{\mathrm{T}}\mathbf{R}\dot{\boldsymbol{\varepsilon}}_{y(t)}-[\boldsymbol{\varepsilon}_{y(t)}-\boldsymbol{\varepsilon}_{y(t-h)}]^{\mathrm{T}}\mathbf{R}[\boldsymbol{\varepsilon}_{y(t)}-\boldsymbol{\varepsilon}_{y(t-h)}]+2\boldsymbol{\varepsilon}_{y(t)}^{\mathrm{T}}\mathbf{P}_1\dot{\boldsymbol{\varepsilon}}_{y(t)}+\theta\boldsymbol{\varepsilon}_{y(t)}^{\mathrm{T}}\mathbf{S}\boldsymbol{\varepsilon}_{y(t)}$, respectively. Based on these terms ($\overline{\boldsymbol{\eta}}_1^{\mathrm{T}}\boldsymbol{\Phi}_1\overline{\boldsymbol{\eta}}_1$ and $\overline{\boldsymbol{\eta}}_2^{\mathrm{T}}\boldsymbol{\Phi}_2\overline{\boldsymbol{\eta}}_2$), the LMI conditions (40)–(41) and (52) are expressed as

$$\dot{V}_{o1} \le -\lambda\theta\|\overline{\boldsymbol{\eta}}_1\|^2+\lambda_{\max}(\boldsymbol{\Phi}_2)\|\overline{\boldsymbol{\eta}}_2\|^2 \tag{53}$$

To ensure convergence of the proposed observer, the following lemma is introduced:

Lemma 1 : *Given the term* $\mathbf{R}$ *as a positive definite matrix, there exists a positive parameter* $\bar{\varepsilon}$ *such that the following argument holds:*

$$\begin{aligned}&\bar{\varepsilon}\lambda_{\max}(\mathbf{R})\left[\left\|\boldsymbol{\varepsilon}_{y(t)}\right\|^2+\left\|\boldsymbol{\varepsilon}_{x(t)}\right\|^2\right] \\ &\ge h\textstyle\int_{-h}^{0}\int_{t+r}^{t}\dot{\boldsymbol{\varepsilon}}_{y(s)}^{\mathrm{T}}\mathbf{R}\dot{\boldsymbol{\varepsilon}}_{y(s)}dsdr \ge 0\end{aligned} \tag{54}$$

where $\mathbf{R}$ is a positive-definite matrix, $h>0$ is a constant delay, and $\bar{\varepsilon}$ is a positive parameter.

Proof of Lemma 1, the following inequality is satisfied.

$$h\int_{-h}^{0}\int_{t+r}^{t}\dot{\boldsymbol{\varepsilon}}_{y(s)}^{\mathrm{T}}\mathbf{R}\dot{\boldsymbol{\varepsilon}}_{y(s)}dsdr \le \lambda_{\max}(\mathbf{R})h\int_{-h}^{0}\int_{t+r}^{t}\dot{\boldsymbol{\varepsilon}}_{y(s)}^{\mathrm{T}}\dot{\boldsymbol{\varepsilon}}_{y(s)}dsdr \tag{55}$$

Taking into account that the expression $h\int_{h}^{0}\int_{t+r}^{t}\dot{\boldsymbol{\varepsilon}}_{y(s)}^{\mathrm{T}}\dot{\boldsymbol{\varepsilon}}_{y(s)}dsdr$ can be rewritten as follows [32]:

$$h\int_{-h}^{0}\int_{t+r}^{t}\dot{\boldsymbol{\varepsilon}}_{y(s)}^{\mathrm{T}}\dot{\boldsymbol{\varepsilon}}_{y(s)}dsdr = h\int_{t-h}^{t}(h+s-t)\dot{\boldsymbol{\varepsilon}}_{y(s)}^{\mathrm{T}}\dot{\boldsymbol{\varepsilon}}_{y(s)}ds \tag{56}$$

In addition, the function $h\int_{t-h}^{t}(h+s-t)ds$ in (56) is bounded and monotonically increases over the interval $[(t-h),\ t]$ (see [32] for further detail). This implies that expression $h\int_{t-h}^{t}(h+s-t)ds$ is convex. Using the Hermite-Hadamard inequality [34], we obtain:

$$\begin{aligned}\frac{1}{h}\int_{t-h}^{t}(h+s-t)\dot{\boldsymbol{\varepsilon}}_{y(s)}^{\mathrm{T}}\dot{\boldsymbol{\varepsilon}}_{y(s)}ds &\le \frac{1}{2}(h+s-t) \\ \times\dot{\boldsymbol{\varepsilon}}_{y(s)}^{\mathrm{T}}\dot{\boldsymbol{\varepsilon}}_{y(s)}|_{s=t}&+(h+s-t)\dot{\boldsymbol{\varepsilon}}_{y(s)}^{\mathrm{T}}\dot{\boldsymbol{\varepsilon}}_{y(s)}|_{s=t-h}\end{aligned} \tag{57}$$

Substituting the term $\dot{\boldsymbol{\varepsilon}}_{y(t)}$ from (46) into (57), we obtain:

$$\begin{aligned}&\int_{t-h}^{t}(h+s-t)\dot{\boldsymbol{\varepsilon}}_{y(s)}^{\mathrm{T}}\dot{\boldsymbol{\varepsilon}}_{y(s)}ds \le \frac{h^2}{2}\left[(\theta\mathbf{A}_1-\bar{\mathbf{K}}_{\mathbf{w}})\boldsymbol{\varepsilon}_{x(t)}+\bar{\mathbf{K}}_{\mathbf{w}}\boldsymbol{\varepsilon}_{y(t)}\right]^{\mathrm{T}} \\ &\times\left[(\theta\mathbf{A}_1-\bar{\mathbf{K}}_{\mathbf{w}})\boldsymbol{\varepsilon}_{x(t)}+\bar{\mathbf{K}}_{\mathbf{w}}\boldsymbol{\varepsilon}_{y(t)}\right] \le \bar{\varepsilon}\left[\left\|\boldsymbol{\varepsilon}_{y(t)}\right\|^2+\left\|\boldsymbol{\varepsilon}_{x(t)}\right\|^2\right]\end{aligned} \tag{58}$$

where $\bar{\varepsilon}=h^2\sup\left\{(\theta\mathbf{A}_1-\bar{\mathbf{K}}_{\mathbf{w}})^{\mathrm{T}}(\theta\mathbf{A}_1-\bar{\mathbf{K}}_{\mathbf{w}}),\bar{\mathbf{K}}_{\mathbf{w}}^{\mathrm{T}}\bar{\mathbf{K}}_{\mathbf{w}}\right\}$, this ends the proof of Lemma 1. Invoking above Lemma 1, the proposed Lyapunov–Krasovskii functional in (48) satisfies:

$$\begin{aligned}&\left[\lambda_{\min}(\mathbf{P})\left\|\boldsymbol{\varepsilon}_{x(t)}\right\|^2+\lambda_{\min}(\mathbf{P}_1)\left\|\boldsymbol{\varepsilon}_{y(t)}\right\|^2\right] \le V_{o1} \le \Big[[\lambda_{\max}(\mathbf{P}) \\ &+\bar{\varepsilon}\lambda_{\max}(\mathbf{R})]\left\|\boldsymbol{\varepsilon}_{x(t)}\right\|^2+[\lambda_{\max}(\mathbf{P}_1)+\bar{\varepsilon}\lambda_{\max}(\mathbf{R})]\left\|\boldsymbol{\varepsilon}_{y(t)}\right\|^2\Big]\end{aligned} \tag{59}$$

Now, provided that the LMI conditions (40)–(41) are satisfied, the first and second terms of (53) can be expressed as:

$$\begin{aligned}-\lambda\theta\|\overline{\boldsymbol{\eta}}_1\|^2 &= -\lambda\theta\left[\left\|\boldsymbol{\varepsilon}_{x(t)}\right\|^2+\left\|\boldsymbol{\varepsilon}_{y(t)}\right\|^2\right], \\ \lambda_{\max}(\boldsymbol{\Phi}_2)\|\overline{\boldsymbol{\eta}}_2\|^2 &\le \lambda_{\max}(\boldsymbol{\Phi}_2)\left[\left\|\boldsymbol{\varepsilon}_{x(t)}\right\|^2+\left\|\boldsymbol{\varepsilon}_{y(t)}\right\|^2\right]\end{aligned} \tag{60}$$

Consequently, these terms can be bounded as follows.

$$-\lambda\theta\|\overline{\boldsymbol{\eta}}_1\|^2+\lambda_{\max}(\boldsymbol{\Phi}_2)\|\overline{\boldsymbol{\eta}}_2\|^2 \le -aV_{o1} \tag{61}$$

where $a>0$ denotes a positive constant. Note that because the LMI condition (41) holds, this implies that $\lambda_{\max}(\boldsymbol{\Phi}_2)$ can only be negative or zero [35]. Therefore,

$$\lambda_{\max}(\boldsymbol{\Phi}_2)\|\overline{\boldsymbol{\eta}}_2\|^2 \le \lambda_{\max}(\boldsymbol{\Phi}_2)\|\overline{\boldsymbol{\eta}}_1\|^2 \tag{62}$$

By using the vectors $\overline{\boldsymbol{\eta}}_1$ and (62), we can rewrite (61) as

$$\bar{\sigma}^2\left[\left\|\boldsymbol{\varepsilon}_{x(t)}\right\|^2+\left\|\boldsymbol{\varepsilon}_{y(t)}\right\|^2\right] \ge V_{o1} \tag{63}$$

where $\bar{\sigma}=\sqrt{\frac{[\lambda\theta+\lambda_{\max}(\boldsymbol{\Phi}_2)]}{a}}$ denotes a positive constant. Accordingly, the following inequality holds: $\left[\left\|\boldsymbol{\varepsilon}_{x(t)}\right\|+\left\|\boldsymbol{\varepsilon}_{y(t)}\right\|\right]^2 \ge \left\|\boldsymbol{\varepsilon}_{x(t)}\right\|^2+\left\|\boldsymbol{\varepsilon}_{y(t)}\right\|^2$. By exploiting this inequality, (63) can be rewritten as

$$\bar{\sigma}^2\left[\left\|\boldsymbol{\varepsilon}_{x(t)}\right\|+\left\|\boldsymbol{\varepsilon}_{y(t)}\right\|\right]^2 \ge V_{o1} \tag{64}$$

Now, we can bound (53) using (61) as $\dot{V}_{o1} \le -aV_{o1}$, solving for the term V_{o1}, which leads to

$$V_{o1}=V_{o1}(0)e^{-at} \tag{65}$$

From (65), as $t \to \infty$, $V_{o1} \to 0$. This implies that:

$$\left\|\boldsymbol{\varepsilon}_{x(t)}\right\| + \left\|\boldsymbol{\varepsilon}_{y(t)}\right\| \geq 0 \tag{66}$$

For the ideal case, the external disturbances and parametric uncertainties were assumed to be zero. This implies that (66) becomes $\left\|\boldsymbol{\varepsilon}_{x(t)}\right\| + \left\|\boldsymbol{\varepsilon}_{y(t)}\right\| = 0$. Therefore, under an unperturbed condition, the state estimation errors of the proposed observer converge exponentially to the origin.

2) Study of the perturbed system: To aid in the performance recovery analysis of the resulting closed-loop system under the bounded control law (15) and perturbation, we inject the control law $\boldsymbol{\tau}$ into (37)-(38), resulting in the perturbed closed-loop dynamics.

$$\begin{cases} \dot{\bar{\boldsymbol{\chi}}}(t) = \bar{\mathbf{A}}\bar{\boldsymbol{\chi}} + \bar{\mathbf{B}}_{\bar{\boldsymbol{\chi}}(t)}\boldsymbol{\tau} + \bar{\mathbf{D}}\bar{\boldsymbol{\delta}}(t) \\ \dot{\hat{\bar{\boldsymbol{\chi}}}}(t) = \bar{\mathbf{A}}\hat{\bar{\boldsymbol{\chi}}}(t) + \bar{\mathbf{B}}^{\star}_{\hat{\boldsymbol{\chi}}(t)}\boldsymbol{\tau} + \boldsymbol{\Delta}_{\theta}\mathbf{K}^{\star}[\mathbf{w}(t) - \bar{\mathbf{C}}\hat{\bar{\boldsymbol{\chi}}}(t)] \\ \dot{\mathbf{w}}(t) = \bar{\mathbf{C}}[\bar{\mathbf{A}}\hat{\bar{\boldsymbol{\chi}}}(t) + \bar{\mathbf{B}}^{\star}_{\hat{\boldsymbol{\chi}}(t)}\boldsymbol{\tau}] + \mathbf{K}_{\mathbf{w}}[\mathbf{w}(t) - \bar{\mathbf{C}}\hat{\bar{\boldsymbol{\chi}}}(t)] \end{cases} \tag{67}$$

where the tracking error $\mathbf{e}_1(t)$ (assuming full-state measurements) becomes $\mathbf{e}_1^{\star}(t) = \boldsymbol{\eta}_d(t) - \hat{\boldsymbol{\eta}}(t)$ and $\hat{\boldsymbol{\eta}}(t)$ are the continuous state estimates.

It is noteworthy that the term $\boldsymbol{\tau}$ (designed in Section III) satisfies conditions (i)–(ii) of Assumption 2 in [31] by design. Based on the transformations in (46) and (67), the resulting closed-loop error dynamics can be rewritten as

$$\begin{aligned} \dot{\boldsymbol{\varepsilon}}_{x(t)} = \boldsymbol{\Delta}_{\theta}^{-1}[\bar{\mathbf{A}} - \boldsymbol{\Delta}_{\theta}\mathbf{K}^{\star}\bar{\mathbf{C}}]\boldsymbol{\Delta}_{\theta}\boldsymbol{\varepsilon}_{x(t)} + \boldsymbol{\Delta}_{\theta}^{-1}\boldsymbol{\Delta}_{\theta}\mathbf{K}^{\star}\bar{\mathbf{C}}\boldsymbol{\Delta}_{\theta}\boldsymbol{\varepsilon}_{y(t)} \\ + \boldsymbol{\Delta}_{\theta}^{-1}\boldsymbol{\Phi}(\cdot)\boldsymbol{\tau} + \boldsymbol{\Delta}_{\theta}^{-1}\bar{\mathbf{D}}\bar{\boldsymbol{\delta}} \\ \dot{\boldsymbol{\varepsilon}}_{y(t)} = \theta\mathbf{A}_1\boldsymbol{\varepsilon}_{x(t)} - \bar{\mathbf{K}}_{\mathbf{w}}\boldsymbol{\varepsilon}_{x(t)} + \bar{\mathbf{K}}_{\mathbf{w}}\boldsymbol{\varepsilon}_{y(t)} \end{aligned} \tag{68}$$

Subsequently, to investigate the performance recovery of the resulting perturbed closed-loop error dynamics (resulting from the proposed output feedback S$^+$RISE controller), we consider the following composite Lyapunov–Krasovskii functional candidate:

$$V_{co} = V_c^{\star}(\mathbf{z}^{\star}, t) + V_{o1}^{\star} \tag{69}$$

where $V_c^{\star}(\mathbf{z}^{\star}, t)$ and $V_{o1}^{\star}$ are similar to $V_c(\mathbf{z}, t)$ and V_{o1}, respectively. However, $V_c^{\star}(\mathbf{z}^{\star}, t)$ and $V_{o1}^{\star}$ satisfy the following arguments, instead of (29) and (59), respectively:

$$\begin{aligned} \frac{1}{2}\min\{1, \kappa\}\tanh^2\left[\left\|\mathbf{z}^{\star}\right\|_{in}\right] \leq V_c^{\star}(\mathbf{z}^{\star}, t) \\ \leq \max\left\{\frac{1}{2}\kappa(\hat{\boldsymbol{\eta}}), \frac{3}{2}\right\}\left\|\mathbf{z}^{\star}\right\|_{s^{\star}}^2, \quad \bar{c}_1\|\boldsymbol{\varsigma}\|_{s^{\star}} \leq V_{o1}^{\star} \leq \bar{c}_2\|\boldsymbol{\varsigma}\|_{s^{\star}} \end{aligned} \tag{70}$$

with $\|\cdot\|_{s^{\star}} = \sup\limits_{t\in\mathbb{R}_{\geqslant 0}} \|\cdot\|$, $\|\cdot\|_{in} = \inf\limits_{t\in\mathbb{R}_{\geqslant 0}} \|\cdot\|$, $\mathbf{z}^{\star}$ is a function of $\mathbf{e}_1^{\star}(t)$, $\boldsymbol{\varsigma}$ is a function of $\{\boldsymbol{\varepsilon}_{x(t)}, \boldsymbol{\varepsilon}_{y(t)}, \dot{\boldsymbol{\varepsilon}}_{y(t)}\}$, $\bar{c}_1 > 0$, and $\bar{c}_2 > 0$. The first time-derivative of (69) yields

$$\dot{V}_{co} = \dot{V}_c^{\star}(\mathbf{z}^{\star}, t) + \dot{V}_{o1}^{\star} \tag{71}$$

By exploiting the result in (35) and replacing $\boldsymbol{\eta}$ with $\hat{\boldsymbol{\eta}}$, (71) can be upper-bounded as follows:

$$\dot{V}_{co} \leq -\left[\gamma - \frac{\rho^2(\|\mathbf{r}_a^{\star}\|)}{2(1 + 3K_{\min})}\right]\|\mathbf{r}_a^{\star}\|^2 + \dot{V}_{o1}^{\star} \tag{72}$$

where $\mathbf{r}_a^{\star}$ is a function of $\mathbf{e}_1^{\star}(t)$. Similarly, using the result of (53), $\dot{V}_{o1}^{\star}$ can be bounded as follows:

$$\dot{V}_{o1}^{\star} \leq -\lambda\theta\|\bar{\boldsymbol{\eta}}_1\|^2 + \lambda_{\max}(\boldsymbol{\Phi}_2)\|\bar{\boldsymbol{\eta}}_2\|^2 + V_{o2}^{\star} \tag{73}$$

where $V_{o2}^{\star} = 2\boldsymbol{\varepsilon}_{x(t)}^{\mathrm{T}}\mathbf{P}\boldsymbol{\Delta}_{\theta}^{-1}[\boldsymbol{\Phi}(\cdot)\boldsymbol{\tau} + \bar{D}\bar{\boldsymbol{\delta}}]$. It is worth noting that the term $V_{o2}^{\star}$ contains saturated feedback control inputs as well as external disturbances. Hence, to deal with the negative effects of these disturbances and parametric uncertainties, the term $V_{o2}^{\star}$ is upper bounded as follows:

$$\begin{aligned} V_{o2}^{\star} \leq 2\lambda_{\max}(\mathbf{P})\Big[L_2\theta^{-[\dim(\boldsymbol{\chi}_2)]} + a_0\|\boldsymbol{\tau}\|\,[L_1\theta^{-[\dim(\boldsymbol{\chi}_2)-1]} \\ + a_0^{\star}\theta^{-[\dim(\boldsymbol{\chi}_2)-2]}]\Big]\left\|\boldsymbol{\varepsilon}_{x(t)}\right\| \end{aligned} \tag{74}$$

where L_1 and L_2 are defined in Remark 5, $a_0 > 0$ and $a_0^{\star} \geq \left\|\boldsymbol{\Phi}(\cdot)\right\| \in \mathbb{R}_{>0}$. Note that all disturbances and uncertainties were replaced with their corresponding upper bounds. Furthermore, the parameter a_0 was designed to deal with any additional high gain that may be generated because of the high magnitude of the parameter θ [13].

Following the same philosophy as in (54)-(64) and considering the worst-case impacts of external disturbances and parametric uncertainties, (73) can be bounded as follows:

$$\dot{V}_{o1}^{\star} \leq -aV_{o1}^{\star} + b\sqrt{V_{o1}^{\star}} \tag{75}$$

where $V_{o2}^{\star}$ is bounded by $V_{o2}^{\star} \leq b\sqrt{V_{o1}^{\star}}$ with $b > 0$.

By introducing the following change in the coordinate $\bar{W}^{\star} = \sqrt{V_{o1}^{\star}}$ and simplifying (75), we obtain:

$$\dot{\bar{W}}^{\star} = \frac{a}{2}\left[-\bar{W}^{\star} + \frac{b}{a}\right] \tag{76}$$

Solving (76) analytically yields $\bar{W}^{\star} = \bar{W}^{\star}(0)e^{-\frac{a}{2}t} + \frac{b}{a}$. Let $\bar{\rho} = \frac{b}{a\bar{\sigma}}$ as $t \to \infty$ and $\bar{W}^{\star} \to \frac{b}{a}$. Accordingly, from (64), we deduce that $\left\|\boldsymbol{\varepsilon}_{x(t)}\right\| + \left\|\boldsymbol{\varepsilon}_{y(t)}\right\| \leq \bar{\rho}$. Therefore, the stability of $V_{o1}^{\star}$ is ensured. This result implies that the composite functional V_{co} is stable and that the estimation and tracking errors are bounded. However, it is worth pointing out that the proposed CDO estimation error converges exponentially towards a ball $\mathcal{B}_{\bar{\rho}}$, whose radius is $\bar{\rho} = \frac{b}{\bar{\sigma}a}$ $\left(\text{where } a = \left|\frac{-\lambda\theta + \lambda_{\max}(\boldsymbol{\Phi}_2)}{\sup\left\{\lambda_{\max}(\mathbf{P}), \lambda_{\max}(\mathbf{P}_1)\right\} + \bar{\varepsilon}\lambda_{\max}(\mathbf{R})}\right|,\ b = \frac{2\lambda_{\max}(\mathbf{P})[L_2\theta^{-[\dim(\boldsymbol{\chi}_2)]} + \theta^{-[\dim(\boldsymbol{\chi}_2)-1]}a_0\|\boldsymbol{\tau}\|]}{\sqrt{\lambda_{\min}(\mathbf{P})}}\right)$, which can be made small enough as long as the observer's high-gain parameter θ is designed sufficiently large. This is due to the effects of perturbations and parametric uncertainties, considered in this perturbed worst-case analysis. The perturbations and parametric uncertainties may include the measurement noise from the sensors (depth and IMU sensors), the inherent nonlinear behavior of the propellers, the computational accuracy, etc. For this reason, the overall resulting closed-loop error dynamics under bounded control (15) and perturbation converges and remains within a region of attraction $\mathcal{A}_{\mathbb{R}} = \mathcal{S}_{\mathcal{D}}^{\star} \times \mathcal{B}_{\bar{\rho}}^{\star}$, very close to zero.

Remark 6 : *The result in [31] can be easily exploited to prove that $\mathcal{A}_{\mathbb{R}}$ can be extended to include any initial condition. However, this result may be difficult to achieve in real-time marine applications because of hardware limitations (e.g., actuator saturation). Furthermore, by exploiting the results in [31], the closeness of the resulting closed-loop trajectories with and without an observer can be easily shown.*

This article has been accepted for publication in IEEE Transactions on Control Systems Technology. This is the author's version which has not been fully edited and content may change prior to final publication. Citation information: DOI 10.1109/TCST.2022.3224321

V. REAL-TIME EXPERIMENTAL RESULTS

In this section, we present and discuss the real-time experimental results obtained from the application of the proposed observer-based robust controller to a *Leonard* underwater vehicle. In the following section, some implementation issues are highlighted before detailing the results obtained.

A. Some Real-Time Implementation Issues

The previous sections presented the theoretical design of the proposed S$^+$RISE and CDO for the six DOF of the vehicle. For the real-time tests using our vehicle, we will focus on controlling two DOF: one transnational DOF (depth) and one rotational DOF (yaw), for the following technical reasons without the loss of generality. (i) The yaw (ψ) of most underwater vehicles, including our vehicle prototype, is sensitive and difficult to control. From a practical point of view, several marine operations require manipulating the yaw of the vehicles. For example, oceanography and dam wall inspection [30]. (ii) The measurement of the depth (z) DOF is too noisy, which is mainly caused by the pressure sensor. (iii) The surge (x) and sway (y) DOF of the vehicle are not measurable and unobservable, whereas the roll (ϕ) and pitch (ϑ) are passively stable. During the tests, the vehicle tracked the desired depth and yaw as accurately as possible, despite the effects of internal and external disturbances, parametric uncertainties, unmodelled dynamics, and unpredictable operating environments. Controlling the depth and yaw of underwater vehicles plays a crucial role in various marine applications. All the proposed real-time experimental tests in this study were carried out in LIRMM's testing pool. A laptop computer with an Intel Core i7-5600U 2.6 GHz CPU, 16 GB of memory (RAM), and the Windows 10 operating system was used to control the vehicle. The code was written in the C++ language in Visual Studio 2015. A video of the complete set of real-time tests can be found in **https://youtu.be/YR8x1aOY1NY**

B. Proposed Real-Time Experimental Scenarios

In order to investigate the performance and efficiency of the proposed S$^+$RISE, compared to the standard RISE controller, as well as the improvement achieved by integrating the proposed CDO, we propose the following experimental scenarios:

1) Scenario 1 (Nominal Case): The objective of this scenario is to tune the gain of each controller online and independently. For a fair comparison, when the best tracking performance was obtained, the gains were maintained for all forthcoming scenarios. Note that, in this scenario, the robot is only subjected to internal perturbations (sensor noise).

2) Scenario 2 (Robustness Towards Parametric Uncertainties): The robustness of each control law is assessed in this scenario when the robot is subjected to parametric uncertainties (e.g., change in mass/weight, damping, and buoyancy).

3) Scenario 3 (External Disturbance Rejection): The main goal of this scenario was to investigate the ability of the control laws to reject real-life external disturbances and to maintain the robot on the desired trajectory. Some of these real-life disturbances in marine applications may include collisions with marine structures, time-varying currents, tether drag, etc.

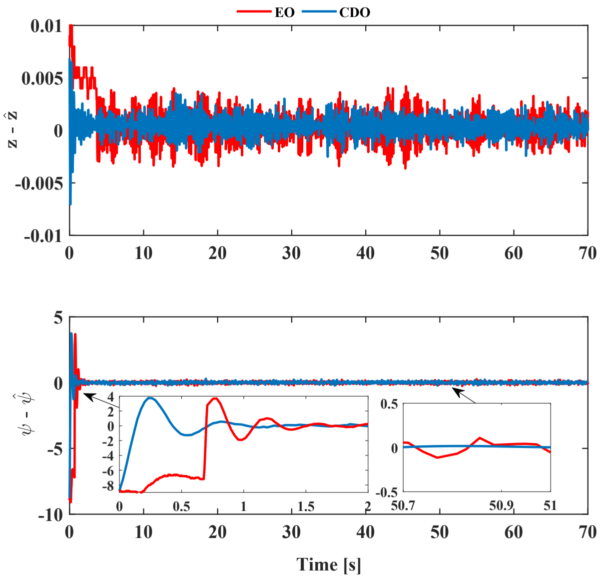

Fig. 2. Observation experimental results comparing our proposed CDO with EO [36].

C. Obtained Observation Results

The main aim of this experimental scenario is to show the obtained observation results of our proposed CDO compared to an extended state high-gain observer (EO) recently proposed in [36]. From Fig. 2, we observe that the proposed CDO converges faster to the origin. In addition, it mitigates the peaking problem during the transient phase, particularly the yaw behavior. Furthermore, the proposed CDO minimizes the observation errors of the depth and yaw by 45.40% and 24.72%, respectively, when compared to EO based on the root mean square error (RMSE) performance index.

D. Obtained Results of Scenario 1:

In these experiments, the *Leonard* ROV tracked the desired time-varying depth and yaw trajectories simultaneously, starting from the surface of the testing pool. Focusing on depth tracking, the robot dives vertically downwards to a maximum depth of 0.3 m from the surface and stays at this level for approximately 10 s. Then, the robot decreases its depth by 0.1 m and stabilizes at this new level within approximately 5 s until the end of the mission. In the case of yaw tracking, the robot changes its course from an initial yaw of 0° to a desired yaw of $+60^\circ$ in 5 s. Then, it maintains this heading for the next 12 s. Finally, the robot changes its heading from $+60^\circ$ to -60° in 5 s, and then maintains this orientation for the remaining time of the experiment. It should be noted that during this experiment, neither external disturbances nor parametric uncertainties were considered. The proposed observer and control-law parameters tuned for this test are summarized in TABLE II. These parameters were maintained in all subsequent real-time experiments. The tuned parameters of the proposed observer were obtained based on LMI.

From Fig 3 (top plots), we can observe better depth tracking for the proposed CDO-S$^+$RISE compared to S$^+$RISE and

This article has been accepted for publication in IEEE Transactions on Control Systems Technology. This is the author's version which has not been fully edited and content may change prior to final publication. Citation information: DOI 10.1109/TCST.2022.3224321

TABLE II
PROPOSED OBSERVER/CONTROL DESIGN PARAMETERS

Depth	S$^+$RISE	$k_{0d} = 2.450$	$\beta_d = 3.750$	$\bar{\lambda}_{0d} = 0.450$
		$\varepsilon_{1d} = 0.010$	$\varepsilon_{2d} = 1 \times 10^{-5}$	$\varepsilon_{3d} = 0.240$
		$\delta_{1d} = 0.850$	$\delta_{2d} = 0.500$	$\alpha_d = 16.500$
		$\mu_{1d} = 0.950$	$\mu_{2d} = 1.000$	
	CDO	$K_d^\star = 16.500$	$K_{w_d} = 0.100$	$\theta_d = 24.390$
Yaw	S$^+$RISE	$k_{0\psi} = 0.720$	$\beta_\psi = 0.050$	$\bar{\lambda}_{0\psi} = 0.060$
		$\varepsilon_{1\psi} = 0.014$	$\varepsilon_{2\psi} = 1 \times 10^{-5}$	$\varepsilon_{3\psi} = 0.060$
		$\delta_{1\psi} = 0.600$	$\delta_{2\psi} = 0.700$	$\alpha_\psi = 1.100$
		$\mu_{1\psi} = 0.600$	$\mu_{2\psi} = 0.700$	
	CDO	$K_\psi^\star = 0.200$	$K_{w_\psi} = 0.100$	$\theta_\psi = 24.390$

TABLE III
TRACKING PERFORMANCE (RMSE) AND INTEGRAL OF CONTROL INPUTS (INT) INDICES FOR THE THREE CONTROLLERS

Index	Scenario	RISE [1]	S$^+$RISE	CDO-S$^+$RISE
RMSE$_{depth}$ [$\times 10^{-2}$ m]	$S1$	1.220	0.719	0.345
	$S2-C1$	1.080	1.030	0.553
	$S2-C2$	1.280	1.120	0.715
	S3	–	–	1.940
RMSE$_{yaw}$ [$\times 10^{-2}$ deg]	$S1$	2.640	2.220	2.208
	$S2-C1$	2.560	1.536	1.474
	$S2-C2$	3.000	1.740	1.656
	$S3$	–	–	2.540
INT$_{depth}$	$S1$	291.000	290.000	296.000
	$S2-C1$	66.900	83.400	66.900
	$S2-C2$	364.000	372.000	385.000
	$S3$	–	–	279.000
INT$_{yaw}$	$S1$	22.500	21.800	17.000
	$S2-C1$	22.500	19.400	19.700
	$S2-C2$	19.000	19.600	19.900
	$S3$	–	–	21.300

RISE controllers, although the experiment was conducted under nominal conditions. The yaw tracking of the proposed CDO-S$^+$RISE controller is approximately similar to that of the proposed S$^+$RISE controller, as confirmed by the error plots (middle plots) in Fig. 3. The numerical quantification of the depth- and yaw-tracking errors for all three controllers is summarized in TABLE III. The computations are based on the RMSE, expressed as $\text{RMS}[\mathbf{e}(t)]_{robot position/attitude} = [\frac{1}{T_f}\int_0^{T_f} \|\mathbf{e}(t)\|^2 dt]^{\frac{1}{2}}$, where $\mathbf{e}(t)$ is the position/attitude tracking error and T_f denotes the duration of the experimental test. According to the obtained results, the RMSE index clearly shows the improvement achieved by the proposed CDO-S$^+$RISE controller with respect to the proposed S$^+$RISE controller. The bottom plots of Fig. 3 shows the evolution of control inputs. Despite the better depth tracking performance of the proposed CDO-S$^+$RISE control scheme, one can quickly notice that it has approximately the same energy consumption compared to the standard RISE controller. Similarly, integrating the proposed CDO with S$^+$RISE decreases the yaw tracking error. Furthermore, it reduces the control effort, as shown in Fig. 3 (bottom). However, it is worth noting that the slightly high control inputs from the proposed CDO-S$^+$RISE scheme at the beginning of the real-time test were caused by the initial tracking error combined with the observation error. Despite these errors, the proposed CDO-S$^+$RISE scheme converged exponentially to the desired track.

To quantify the control efforts numerically, we propose using the integral of the control input index (INT), formulated as $\text{INT}[\boldsymbol{\tau}]_{robot position/attitude} = \int_{t_i}^{t_f} \|\boldsymbol{\tau}(t)\|^2 dt$, where $\boldsymbol{\tau}(t)$ denotes the vector of the position/attitude control input, t_i represents the initial time when the robot converges to $\boldsymbol{\eta}_d(t)$ and t_f is the final time at the end of the mission. TABLE III summarizes the results obtained from the INT index computations in this experimental test.

E. Obtained Results of Scenario 2:

In this scenario, another implementation issue arises apart from those previously mentioned. This problem results in the integration of parametric variations in robot dynamics without changing its physical structure. To this end, we proposed dividing this scenario into two separate cases as follows:

1) Case 1: To introduce a variation in the matrix $\mathbf{M}_{\boldsymbol{\eta}}^\star(\cdot)$ of the robot dynamics (7) without changing its physical configuration, we propose the following: First, a thread of known length and negligible mass is tied from one end at the base of the robot and from the other end to a payload representing 4% of the robot's weight. When the robot reached the maximum depth (0.3 m), the payload touched the floor of the testing pool. This resulted in a sudden change in the matrix from $\mathbf{M}_{\boldsymbol{\eta}}^\star(\cdot) + \Delta\mathbf{M}_{\boldsymbol{\eta}}^\star(\cdot)$ to $\mathbf{M}_{\boldsymbol{\eta}}^\star(\cdot)$, as shown in Fig. 4. It is worth noting that this enables the assessment of the robustness of all three autonomous control algorithms towards a reject variation in the matrix $\mathbf{M}_{\boldsymbol{\eta}}^\star(\cdot)$ of the robot's dynamics, as well as their efficiency in real-life tasks. Therefore, this can be interpreted as the task of carrying tools/samples by the robot from the surface to a deep-sea area (or seabed). Once the payload was well attached, the robot tracked the desired time-varying trajectories, as shown in Fig. 5 (top). As the robot moved down to a depth of approximately 0.25 m, the attached load canceled out its effect on the robot because it suddenly lay on the floor of the testing pool. This change causes both the proposed S$^+$RISE and standard RISE controllers to deviate from the desired depth; however, the proposed CDO-S$^+$RISE controller smoothly rejects this effect in less than 2 s. Both the proposed S$^+$RISE and standard RISE controllers oscillate around the desired depth for approximately 3 s and 4.5 s, respectively, before neutralizing the effect, as shown in Fig. 5 (top-left plot). Furthermore, the oscillations of both controllers lead to a coupling effect on yaw tracking, as shown in Fig. 5 (top right plot). When the desired depth reaches 0.2 m, the load becomes suspended again, and changes back to the matrix $\mathbf{M}_{\boldsymbol{\eta}}^\star(\cdot)$ to its initial value. Despite this variation, the proposed CDO-S$^+$RISE control scheme smoothly keeps the robot very close to the desired trajectories, as depicted in Fig. 5 (middle). The bottom plot in Fig. 5 shows the evolution of control inputs versus time.

2) Case 2: This test completes the objective of Scenario 2 by introducing parametric variations in both matrix $\mathbf{D}_{\boldsymbol{\eta}}^\star(\cdot)$ and vector $\mathbf{g}_{\boldsymbol{\eta}}^\star(\cdot)$ of the robot dynamics. Similar to the previous test, we propose introducing variations in both the matrix $\mathbf{D}_{\boldsymbol{\eta}}^\star(\cdot)$ and the vector $\mathbf{g}_{\boldsymbol{\eta}}^\star(\cdot)$ through a physical reconfiguration of the robot's structure as follows: The first step involved

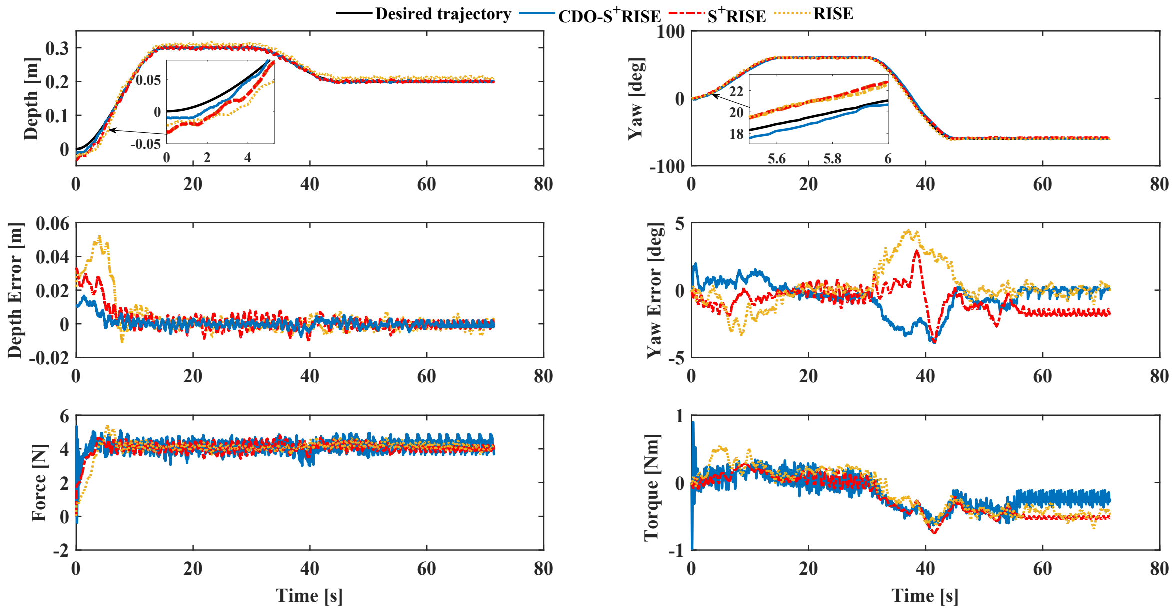

Fig. 3. Obtained experimental results of the proposed schemes compared to RISE [1] for scenario 1 (nominal case).

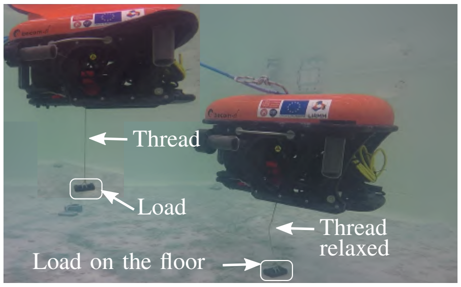

Fig. 4. Illustration of parametric variation for *case 1* of scenario 2.

attaching a $0.45\,\mathrm{m}\times 0.1\,\mathrm{m}$ rigid plastic sheet at the front of the robot (as illustrated in Fig. 6). This modification changes the matrix $\mathbf{D}^{\star}_{\boldsymbol{\eta}}(\cdot)$ by $\Delta\mathbf{D}^{\star}_{\boldsymbol{\eta}}(\cdot) = +90\%$, compared to its nominal value. Subsequently, two floats were mounted on both sides of the robot, as illustrated in Fig. 6. This modification results in a variation of the vector $\mathbf{g}^{\star}_{\boldsymbol{\eta}}(\cdot)$ to $\mathbf{g}^{\star}_{\boldsymbol{\eta}}(\cdot) + \Delta\mathbf{g}^{\star}_{\boldsymbol{\eta}}(\cdot)$, where $\Delta\mathbf{g}^{\star}_{\boldsymbol{\eta}}(\cdot) = +100\%$ with respect to its nominal value. The robot must follow the same reference trajectories as those in the previous scenario. The obtained tracking performance is shown in Fig. 7 (top). The depth tracking errors of the proposed S^{+}RISE and standard RISE controllers increase owing to the parametric uncertainties in the robot dynamics, as shown in Fig. 7 (middle). Although the yaw tracking error of the proposed CDO-S^{+}RISE control scheme is slightly affected, its depth-tracking performance outperforms the other two controllers. The slight yaw-tracking error may be due to the tether of the robot, whose stiffness induces undesired torques during the experiment. The numerical values of the RMS tracking errors are summarized in TABLE III. It is worth noting that the standard RISE, proposed S^{+}RISE, and proposed CDO-S^{+}RISE consume approximately the same amount of energy in this test, as illustrated in Fig. 7 (bottom). This can be confirmed from the numerical values summarized in TABLE III.

Remark 7: *The changes in the matrix* $\mathbf{C}^{\star}_{\boldsymbol{\eta}}(\cdot)$ *of the robot dynamics (7) are not considered in this work, based on assumption* **A2**.

F. Obtained Result of Scenario 3:

Based on the previous description of this scenario, it is possible to generate external disturbances that can affect the robot in a real-life marine mission with an external push, as illustrated in Fig. 8. The magnitude of this push was estimated as approximately 25% of the robot's total weight. We propose to validate the proposed CDO-S^{+}RISE control scheme only in this scenario because it would be almost impossible to make a fair experiment-based comparison because of the following critical issues. The same magnitude of this push needs to be applied to all schemes in real time and under the same conditions (time, point, direction, etc.), which is practically impossible. In addition, according to the previous scenarios, the proposed CDO-S^{+}RISE scheme demonstrated better performance compared to the other two schemes; accordingly, we propose to focus on testing its ability to reject external disturbances.

To apply external disturbances, a long stick was used to push the robot while following the desired trajectories in real time, as illustrated in Fig. 8. As tracking of the desired time-varying depth and heading plays a crucial role in many marine tasks, this external push is applied at several points on the two degrees of freedom of the robot. As can be observed from the curves in Figs. 9 (top left plot) showing the depth tracking, the robot was disturbed at different depth conditions including $0.19\,\mathrm{m}$ (a), $0.30\,\mathrm{m}$ (b), $0.24\,\mathrm{m}$ (c), $0.20\,\mathrm{m}$ $(d_1, d_2, d_3,$ *and* $d_4)$, which can be interpreted as the descent of the robot, a hovering maneuver at a constant depth, a depth change, and

This article has been accepted for publication in IEEE Transactions on Control Systems Technology. This is the author's version which has not been fully edited and content may change prior to final publication. Citation information: DOI 10.1109/TCST.2022.3224321

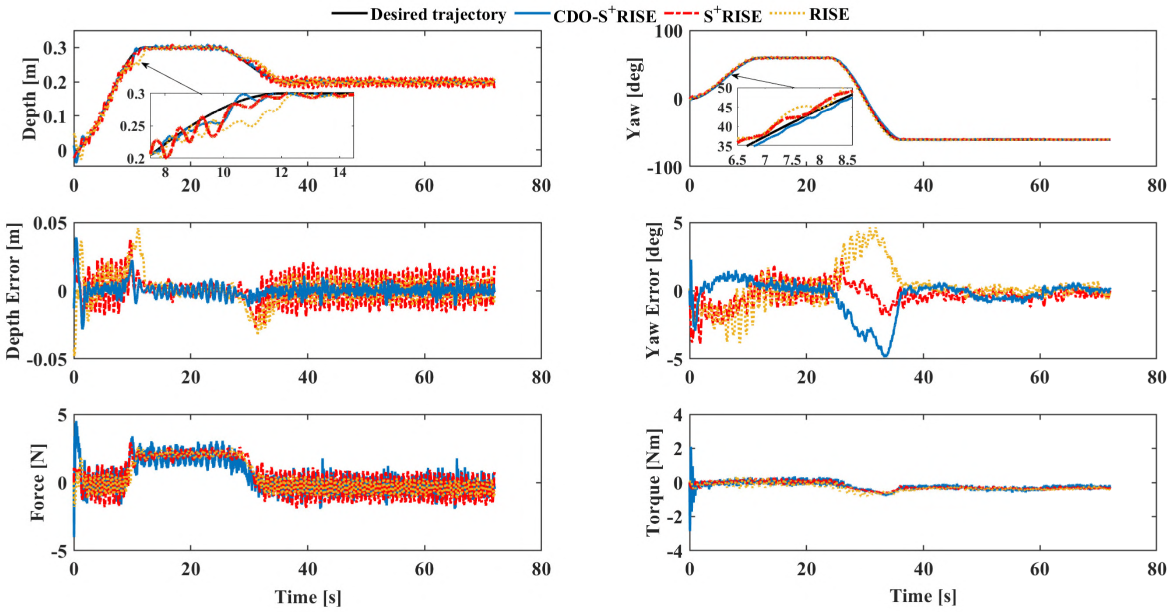

Fig. 5. Obtained experimental results of the proposed schemes compared to RISE [1] for scenario 2-*case 1* (robustness case).

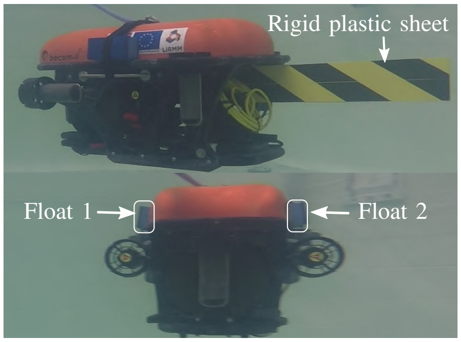

Fig. 6. Illustration of parametric variation for *case 2* of scenario 2.

stabilization at the desired depth, respectively. Similarly, the yaw of the robot is disturbed at the orientations $+60.0°$ (e), $+49.7°$ (f), and $-60.7°$ (g_1 *and* g_2), which correspond to the robot maintaining a constant heading, changing its course, stabilizing, and maintaining a constant heading, respectively (as depicted in the top-right plot of Fig. 9). In both cases, the proposed CDO-S$^+$RISE rejected all external disturbances within a short time (< 2s) and stabilized the robot back around the desired trajectories. It is worth noting that the coupling effects are non-negligible, particularly when the yaw is disturbed, as indicated by the vertical dotted lines on the depth trajectory in Fig. 9 (left)). Even though approximately the same external push is applied along the yaw axis, yaw tracking is less affected than depth tracking, as shown in Fig. 9 (middle). It is worth noting that good tracking is accompanied by slightly higher energy consumption. The bottom plot in Fig. 9 shows the evolution of the control signals generated by the proposed CDO-S$^+$RISE control scheme. TABLES III summarizes the results obtained for the tracking errors and energy consumption.

Remark 8: *Note that, as long as an external disturbance does not cause saturation of the vehicle actuators, both the proposed CDO-S$^+$RISE and S$^+$RISE, in this work, will be able to compensate for such disturbances.*

VI. CONCLUSION AND FUTURE WORK

In this study, a new robust observation-based (CDO-S$^+$RISE) control scheme was proposed. In the first step of the control design, a new saturated super-twisting RISE (S$^+$RISE) controller is proposed to address the tracking problem of autonomous underwater vehicles. Similar to the majority of control algorithms proposed in the literature, the proposed S$^+$RISE requires continuous state measurements. Therefore, a new continuous-discrete time observer (CDO) was proposed and integrated to work in tandem with the proposed S$^+$RISE controller. In addition to estimating the vehicle states and external perturbations, the proposed observer addresses the multirate sampling problem associated with the vehicle sensors. This approach differs from many studies in the literature where the measurements are assumed to be synchronous and continuous. The performance recovery of the overall closed-loop error dynamics was proven. Subsequently, *Leonard* underwater vehicle prototype was used to implement and test the proposed CDO-S$^+$RISE scheme in real time for depth and yaw trackings. Furthermore, the proposed CDO-S$^+$RISE approach was studied and compared to both the proposed S$^+$RISE and standard RISE schemes through different scenarios. The obtained experimental results clearly demonstrate the potential, efficiency, and robustness of the proposed CDO-S$^+$RISE technique. In the future, we may consider integrating an intelligent functionality, such as obstacle avoidance, into the proposed CDO-S$^+$RISE control scheme. Subsequently, the technique is deployed in multi-agent underwater vehicles.

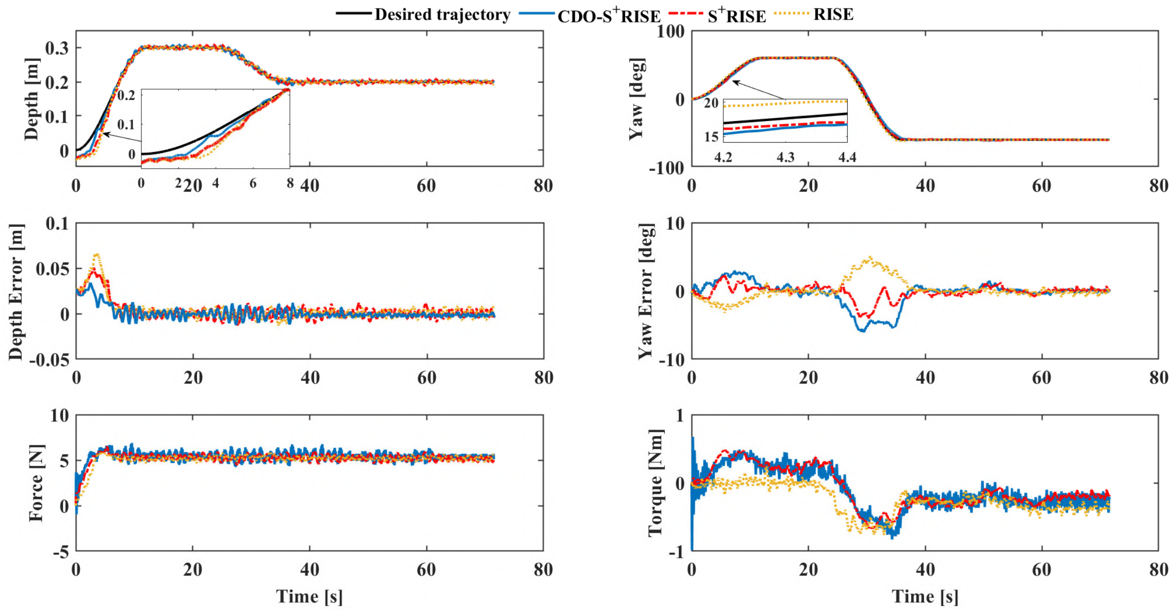

Fig. 7. Obtained experimental results of the proposed schemes compared to RISE [1] for scenario 2-*case 2* (robustness case).

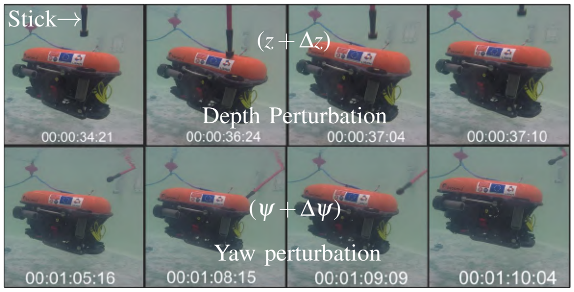

Fig. 8. A sequence of snapshots illustrating external disturbance rejections.

REFERENCES

[1] N. Fischer, D. Hughes, P. Walters, E. M. Schwartz, and W. E. Dixon, "Nonlinear rise-based control of an autonomous underwater vehicle," *IEEE Transactions on Robotics*, vol. 30, no. 4, pp. 845–852, 2014.

[2] I. L. G. Borlaug, K. Y. Pettersen, and J. T. Gravdahl, "Tracking control of an articulated intervention autonomous underwater vehicle in 6dof using generalized super-twisting: Theory and experiments," *IEEE Transactions on Control Systems Technology*, vol. 29, no. 1, pp. 353–369, 2021.

[3] S. Ding, K. Mei, and S. Li, "A new second-order sliding mode and its application to nonlinear constrained systems," *IEEE Transactions on Automatic Control*, vol. 64, no. 6, pp. 2545–2552, 2018.

[4] J. Guerrero, J. Torres, V. Creuze, and A. Chemori, "Trajectory tracking for autonomous underwater vehicle: An adaptive approach," *Ocean Engineering*, vol. 172, pp. 511–522, 2019.

[5] J. Xu, E. Fridman, L. Fridman, and Y. Niu, "Static sliding mode control of systems with arbitrary relative degree by using artificial delay," *IEEE Transactions on Automatic Control*, vol. 65, no. 12, pp. 5464–5471, 2020.

[6] C. A. Martínez-Fuentes, R. Seeber, L. Fridman, and J. A. Moreno, "Saturated lipschitz continuous sliding mode controller for perturbed systems with uncertain control coefficient," *IEEE Transactions on Automatic Control*, vol. 66, no. 8, pp. 3885–3891, 2021.

[7] A. Poznyak, "Stochastic super-twist sliding mode controller," *IEEE Transactions on Automatic Control*, vol. 63, no. 5, pp. 1538–1544, 2017.

[8] R. Wang, S. Wang, Y. Wang, M. Tan, and J. Yu, "A paradigm for path following control of a ribbon-fin propelled biomimetic underwater vehicle," *IEEE Transactions on Systems, Man, and Cybernetics: Systems*, vol. 49, no. 3, pp. 482–493, 2019.

[9] J. M. Escorcia-Hernández, A. Chemori, H. Aguilar-Sierra, and J. A. Monroy-Anieva, "A new solution for machining with ra-pkms: Modelling, control and experiments," *Mechanism and Machine Theory*, vol. 150, p. 103864, 2020.

[10] N. Fischer, Z. Kan, R. Kamalapurkar, and W. E. Dixon, "Saturated rise feedback control for a class of second-order nonlinear systems," *IEEE Transactions on automatic control*, vol. 59, no. 4, pp. 1094–1099, 2013.

[11] F. Sedghi, M. M. Arefi, A. Abooee, and O. Kaynak, "Adaptive robust finite-time nonlinear control of a typical autonomous underwater vehicle with saturated inputs and uncertainties," *IEEE/ASME Transactions on Mechatronics*, vol. 26, no. 5, pp. 2517–2527, 2021.

[12] A. Baruch, Y. Mazal, B. Braginsky, and H. Guterman, "Attitude estimation of auvs based on a network of pressure sensors," *IEEE Sensors Journal*, vol. 20, no. 14, pp. 7988–7996, 2020.

[13] A. Zemouche, F. Zhang, F. Mazenc, and R. Rajamani, "High-gain nonlinear observer with lower tuning parameter," *IEEE Transactions on Automatic Control*, vol. 64, no. 8, pp. 3194–3209, 2019.

[14] H. Hua, Y. Fang, X. Zhang, and B. Lu, "A novel robust observer-based nonlinear trajectory tracking control strategy for quadrotors," *IEEE Transactions on Control Systems Technology*, vol. 29, no. 5, pp. 1952–1963, 2021.

[15] A. Alessandri and F. Boem, "State observers for systems subject to bounded disturbances using quadratic boundedness," *IEEE Transactions on Automatic Control*, vol. 65, no. 12, pp. 5352–5359, 2020.

[16] F. G. de Cossío, M. Nadri, and P. Dufour, "Observer design for nonlinear systems with output transformation," *IEEE Transactions on Automatic Control*, vol. 65, no. 12, pp. 5205–5219, 2020.

[17] J. Yan, J. Gao, X. Yang, X. Luo, and X. Guan, "Position tracking control of remotely operated underwater vehicles with communication delay," *IEEE Transactions on Control Systems Technology*, vol. 28, no. 6, pp. 2506–2514, 2020.

[18] C. Ling and C. Kravaris, "Multirate sampled-data observer design based on a continuous-time design," *IEEE Transactions on Automatic Control*, vol. 64, no. 12, pp. 5265–5272, 2019.

[19] R. Wang, S. Wang, Y. Wang, C. Tang, and M. Tan, "Three-dimensional helical path following of an underwater biomimetic vehicle-manipulator system," *IEEE Journal of Oceanic Engineering*, vol. 43, no. 2, pp. 391–401, 2018.

[20] Q. Liu, M. Liu, Q. Jin, and Y. Liu, "Design of dob-based control system in the presence of uncertain delays for low-order processes," *IEEE Transactions on Control Systems Technology*, vol. 28, no. 2, pp. 558–565, 2020.

[21] M. Farza, M. M'Saad, M. L. Fall, E. Pigeon, O. Gehan, and K. Busawon, "Continuous-discrete time observers for a class of mimo nonlinear

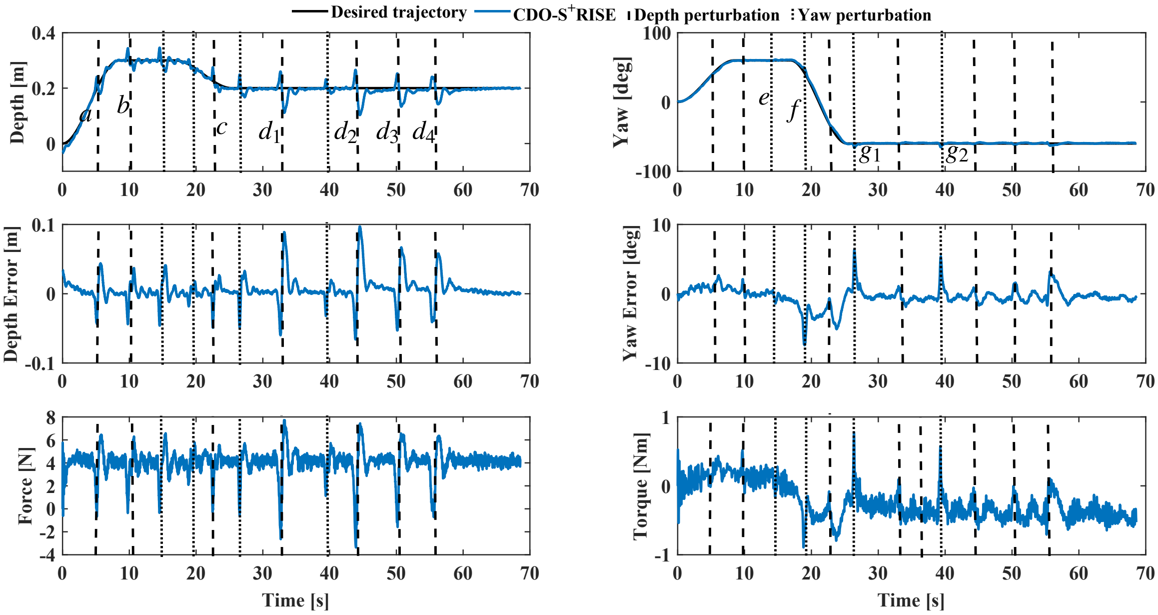

Fig. 9. Obtained experimental results of the proposed CDO-S$^+$RISE scheme for scenario 3 (disturbances rejection).

systems," *IEEE Transactions on Automatic Control*, vol. 59, no. 4, pp. 1060–1065, 2014.

[22] T.-M. Guerra, B. Aguiar, D. Berdjag, and B. Demaya, "Robust estimation for nonlinear continuous-discrete systems with missing outputs: Application to automatic train control," *IEEE Transactions on Control Systems Technology*, pp. 1–7, 2021.

[23] G. C. Karras, P. Marantos, C. P. Bechlioulis, and K. J. Kyriakopoulos, "Unsupervised online system identification for underwater robotic vehicles," *IEEE Journal of Oceanic Engineering*, vol. 44, no. 3, pp. 642–663, 2019.

[24] O. Jaramillo, B. Castillo-Toledo, and S. Di Gennaro, "Robust impulsive observer–based stabilization for uncertain nonlinear systems with sampled–output," *IEEE Control Systems Letters*, vol. 5, no. 3, pp. 845–850, 2021.

[25] A. S. Tijjani, A. Chemori, and V. Creuze, "Robust adaptive tracking control of underwater vehicles: Design, stability analysis, and experiments," *IEEE/ASME Transactions on Mechatronics*, vol. 26, no. 2, pp. 897–907, 2021.

[26] T. I. Fossen, "Guidance, navigation, and control of ships, rigs and underwater vehicles," *Marine Cybernetics. Noruega*, 2002.

[27] J. Bellingham, "Autonomous underwater vehicles (auvs)," *Encyclopedia of Ocean Sciences*, pp. 212–216, 2001.

[28] B. Xian, D. M. Dawson, M. S. de Queiroz, and J. Chen, "A continuous asymptotic tracking control strategy for uncertain nonlinear systems," *IEEE Transactions on Automatic Control*, vol. 49, no. 7, pp. 1206–1211, 2004.

[29] S. A. Ali, A. Christen, S. Begg, and N. Langlois, "Continuous–discrete time-observer design for state and disturbance estimation of electro-hydraulic actuator systems," *IEEE Transactions on Industrial Electronics*, vol. 63, no. 7, pp. 4314–4324, 2016.

[30] E. Campos, A. Chemori, V. Creuze, J. Torres, and R. Lozano, "Saturation based nonlinear depth and yaw control of underwater vehicles with stability analysis and real-time experiments," *Mechatronics*, vol. 45, pp. 49–59, 2017.

[31] J. Lei and H. K. Khalil, "High-gain-predictor-based output feedback control for time-delay nonlinear systems," *Automatica*, vol. 71, pp. 324–333, 2016.

[32] E. Fridman, *Introduction to time-delay systems: Analysis and control*. Springer, 2014.

[33] C. Briat, "Convergence and equivalence results for the jensen's inequality—application to time-delay and sampled-data systems," *IEEE Transactions on Automatic Control*, vol. 56, no. 7, pp. 1660–1665, 2011.

[34] M. E. Özdemir, M. Avcı, and E. Set, "On some inequalities of hermite–hadamard type via m-convexity," *Applied Mathematics Letters*, vol. 23, no. 9, pp. 1065–1070, 2010.

[35] J. Arora, *Introduction to optimum design*. Elsevier, 2004.

[36] D. Chowdhury, Y. K. Al-Nadawi, and X. Tan, "Dynamic inversion-based hysteresis compensation using extended high-gain observer," *Automatica*, vol. 135, p. 109977, 2022.

Auwal Shehu Tijjani received the B.ENG. and M.ENG. degrees from Bayero University, Kano, Nigeria, Univesiti Teknologi Malaysia, Johor Bahru, Malaysia, in 2012 and 2016, respectively. He is currently a PhD student at the University of Montpellier Laboratory of Informatics, Robotics and Microelectronics. His research interests include robust and adaptive control of autonomous underwater vehicles, AUVs.

Ahmed CHEMORI received his M.Sc. and Ph.D. degrees, both in automatic Control from the Grenoble Institute of Technology, Grenoble, France, in 2001 and 2005, respectively. He was a Postdoctoral fellow with the Automatic Control Laboratory, Grenoble, France, 2006. He is currently a Tenured CNRS Researcher in Automatic Control and Robotics with LIRMM Laboratory. His research interests include nonlinear, adaptive and predictive control and its applications in robotics.

Sofiane Ahmed Ali received the B.Sc. degree in electrical engineering from the University of Technology Houari Boumedienne in Algiers in 2001, and the M.Sc. and Ph.D. degrees in electrical and computer engineering from the University of Le Havre, France. in 2004 and 2008, respectively. In 2010, he joined ESIGELEC in Rouen France as an associate professor. His research interests include sliding mode control, nonlinear observers, and fault-tolerant control for mechatronics devices.

Vincent CREUZE received his Ph.D. degree in 2002 from the University Montpellier 2 (France). He is currently a full Professor at the University of Montpellier, attached to the Robotics Department of LIRMM. His research interests include design, modelling, sensing, and control applied to underwater robots for deep archaeological applications or marine biology.